View Article Online
View Journal

Dalton Transactions

An international journal of inorganic chemistry

Accepted Manuscript

This article can be cited before page numbers have been issued, to do this please use: P. Kumar, I. Mondal, R. Kulshreshtha and A. K. Patra, *Dalton Trans.*, 2020, DOI: 10.1039/D0DT02167A.

This is an Accepted Manuscript, which has been through the Royal Society of Chemistry peer review process and has been accepted for publication.

Accepted Manuscripts are published online shortly after acceptance, before technical editing, formatting and proof reading. Using this free service, authors can make their results available to the community, in citable form, before we publish the edited article. We will replace this Accepted Manuscript with the edited and formatted Advance Article as soon as it is available.

You can find more information about Accepted Manuscripts in the Information for Authors.

Please note that technical editing may introduce minor changes to the text and/or graphics, which may alter content. The journal's standard Terms & Conditions and the Ethical guidelines still apply. In no event shall the Royal Society of Chemistry be held responsible for any errors or omissions in this Accepted Manuscript or any consequences arising from the use of any information it contains.

ROYAL SOCIETY OF CHEMISTRY

rsc.li/dalton

Development of Novel Ruthenium(II)-Arene Complexes Displaying Potent Anticancer Effects in Glioblastoma

Priyaranjan Kumar,[a] Indranil Mondal,[b] Ritu Kulshreshtha,[b] and Ashis K. Patra*,[a]

Author address: [a]Department of Chemistry, Indian Institute of Technology Kanpur, Kanpur 208016, Uttar Pradesh, India. E-mail: akpatra@iitk.ac.in

[b]Department of Biochemical Engineering and Biotechnology, Indian Institute of Technology Delhi, Hauz Khas, New Delhi 110 016, India

View Article Online
DOI: 10.1039/D0DT02167A

Abstract

Glioblastoma (GB) is a highly aggressive and malignant brain tumor that is highly resistant to conventional multimodal treatments leading to its abysmal prognosis. We designed two organometallic half-sandwich Ru(II)-η^6-*p*-cymene complexes containing Schiff-base derived from 3-aminoquinoline and 2-hydroxy-benzaldehyde (L1) and 2-hydroxy-naphthaldehyde (L2), namely [Ru(η^6-*p*-cymene)(L1)Cl] (**1**) and [Ru(η^6-*p*-cymene)(L2)Cl] (**2**) and studied their activity on GB cells. Both the complexes were structurally characterized using single-crystal X-ray diffraction showing half-sandwich three-legged piano-stool geometry. We studied the physicochemical behavior, solution speciation, aquation kinetics, and photosubstitution reactions using various spectroscopic methods. The complexes exhibit moderate binding affinity with calf-thymus (CT)-DNA (K_b ~10^5 M^{-1}). The complexes effectively interact with human serum albumin (HSA) (K ~10^5 M^{-1}) with preferential tryptophan binding as determined from synchronous fluorescence studies. The *in vitro* studies showed significant antiproliferative activity against an aggressive human GB cell line LN-229 (IC_{50} = 22.8 μM) with a moderate selectivity relative to the normal mouse fibroblast L929 cells. Notably, [Ru(η^6-*p*-cymene)(L1)Cl] (**1**) have higher selectivity index (S.I.) than [Ru(η^6-*p*-cymene)(L2)Cl] (**2**) or *cis*platin. We evaluated the clonogenic potential of the GB cells using the colony formation assay in the presence of the complex **1**. Excitingly, it shows ~75% inhibition of clonogenic potential at IC_{50} concentration. Complex **1** also effectively lowered the migratory potential of GB cells as accessed from wound healing assay. The studied compound lead to apoptosis of GB cells as evidenced by nuclear condensation, blebbing, and enhanced caspase 3/7 activity with anticipated utility in GB treatment using photochemotherapy.

Introduction

Glioblastoma (GB) is a highly aggressive, malignant, and deadliest form of brain tumor that shows dismal prognosis, with a very high mortality rate [1]. Less than 5% of the patients survive more than 5 years upon a treatment, and average survival is only 3 months without any treatment after diagnosis. GB is probably the most challenging and unique tumor to treat clinically due to its very invasive and somewhat illusive multifocal nature of growth throughout the white matter in the brain [2]. Because of its stealthy and invasive growth through central nervous system (CNS), the surgery remains quite challenging, very often inoperable, and associated with severe cognitive dysfunctions. Over the last 3-4 decades, therapeutic intervention failed to have a noteworthy impact on GB survival. Gamma knife radiosurgery is

View Article Online
DOI: 10.1039/D0DT02167A

one of the technique neurosurgeons uses to remove as well as block the anticipated proliferation of cancerous tissue in white matter tracks [3]. The surgical removal of the tumor is augmented by radiation and cytotoxic chemotherapy. To date, only a few drugs are approved by the US FDA, such as temozolomide (TMZ), bevacizumab, carmustine, and lomustine (Fig. 1). Treatment with temozolomide (Temodar^{TM}), a promiscuous DNA methylating agent, notably demonstrated notable efficacy in combination with radiotherapy. The acquired resistance towards radiation and chemotherapy of GB makes it even more challenging to treat [4]. Despite significant progress in GB genomics, clinical medicine and diagnosis, the combined treatment regimen from surgery and subsequent concomitant radiotherapy and TMZ chemotherapy, its prognosis is still inferior with a median survival of terrifying 14.6 months [5]. Clinically approved DNA damaging drugs (e.g., doxorubicin, irinotecan, etoposide, carmustine and TMZ) remained disappointing for GB targeted therapy [1]. Therefore, combating the aggressive GB tumor chemotherapeutically at the molecular level requires a new drug discovery approach and seems an uphill task for medicinal chemists and clinicians. The molecularly targeted drugs under clinical trial are mostly based on oncogenic receptor tyrosine kinase (RTK) pathways. The PI3K-AKT and RAS oncogenic pathways, along with various growth factors, and their receptors are often targeted with organic inhibitors [1, 5].

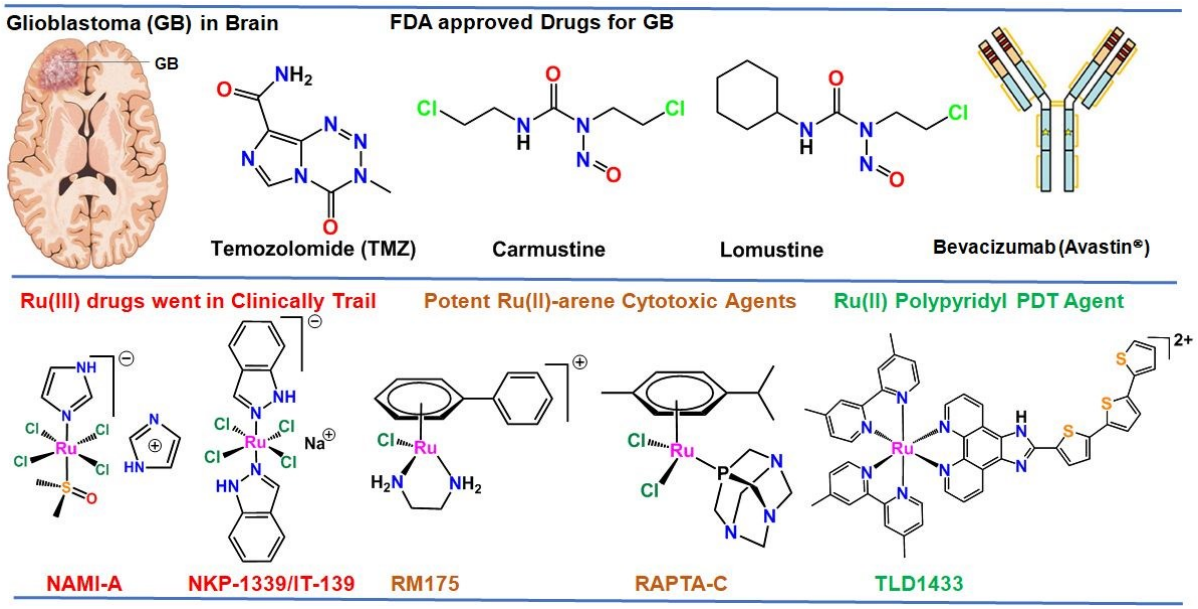

Fig. 1 Top: Schematic representation of glioblastoma (GB) in cerebral hemisphere and FDA approved molecular drugs for glioblastoma after surgical resection. Temozolomide is the current standard of treatment; bevacizumab is a monoclonal antibody (mAb) targeted VEGF-inhibitor. Bottom: Structure of the most successful antimetastatic (NAMI-A) and anticancer ruthenium compounds.

The successful chemotherapy from platins (cisplatin, carboplatin, oxaliplatin) to numerous cancer types envisioned that metallodrugs serendipitously could serve startling efficiency than

organic anticancer drugs [6]. However, the dose-dependent side effects and the acquired drug resistance of platins limits its applicability and simultaneously opens up the opportunity for discovery of new-generation targeted metallodrugs [7−9]. Most of the drugs show side effects because of the poor selectivity index of its target, and the enhanced selectivity index (S.I.) is desirable and directly increases the efficacy of a drug.

Ruthenium is a suitable choice of metal after platinum for metallodrug design towards targeted chemotherapy due to physiologically accessible multiple oxidation states (+II/III), the formation of rigid bonds with hard and soft donor ligands, biocatalytic potentials, transferrin binding as iron mimicking and tunable ligands substitution kinetics similar to Pt(II) drugs [10]. The photochemistry and favorable optical properties of Ru-drugs is fascinating and assists in photodynamic therapy (PDT) or photoactivated chemotherapy (PACT). This is apt for advanced non-invasive spatiotemporally controlled and innovative targeted photo-activated chemotherapy (PACT) modality [11, 12]. The TLD1433 is the first Ru(II)-polypyridyl based PDT agent entered for human clinical trial for treating non-muscle invasive bladder cancer [12b]. The antimetastatic NAMI-A, anticancer NKP-1339 and organometallic Ru(II)-arene complexes namely RM175 [(η^6-biphenyl)Ru(en)Cl]$^+$ (en = ethylenediamine), RAPTA series of complexes [η^6arene)Ru(PTA)Cl_2]$^+$ (PTA = 1,3,5-triaza-7-phosphaadamentane) (Fig. 1) and RDC11 [Ru(phenanthroline)(κ-*C*,*N*-(2-phenyl-pyridine)$(NCMe)_2$]PF_6 have been reported for excellent anticancer activity and significantly reduced side effects and also non-cross resistant with platin drugs [13−15]. Interestingly, the primary molecular targets of these Ru-complexes are not limited to DNA, but also enzyme, genes, and proteins crucial in a postgenomic era, and not entirely driven by cytotoxicity. In the recent years, the screening of a wide spectrum of Ru-arene Schiff-base complexes conjugated with pyridine/quinoline amines with substituted aromatic aldehydes has been reported for overcoming multi-drug resistance (MDR) with apoptosis independent pathways [16, 17].

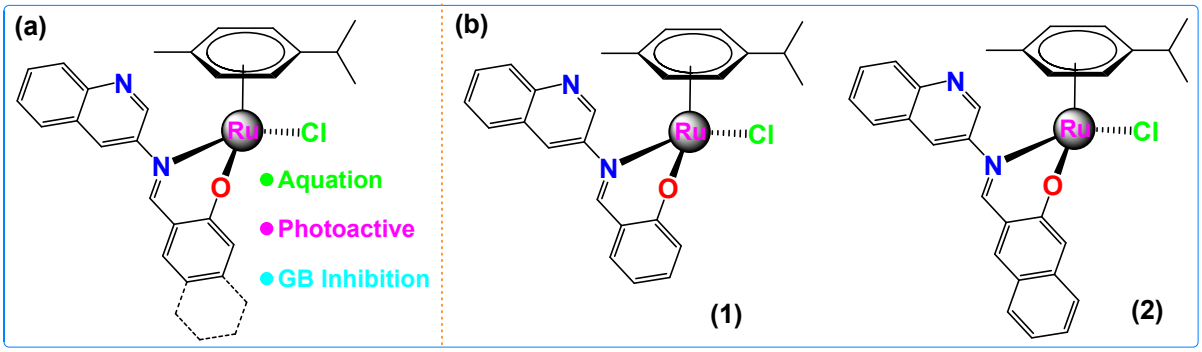

Fig. 2 (a) Design scheme for Ru(II)-arene complexes. (b) [Ru(η^6-*p*-cymene)(L1)Cl] (**1**) and [Ru(η^6-*p*-cymene)(L2)Cl] (**2**) under study.

We designed two Ru(II)-η^6-*p*-cymene half-sandwich complexes using Schiff bases obtained from the conjugation of quinoline amine and 2-hydroxy-benzaldehyde (L1) (**1**) and 2-hydroxy-1-naphthaldehyde (L2) (**2**) (Fig. 2). To our curiosity, we have tested *in vitro* cytotoxicity of these complexes with highly aggressive glioblastoma (GB) cells, LN229, considering the absence of any systematic investigation of cytotoxic metal complexes for GB in literature. We also envision the potential application of PACT or PDT in combination with chemotherapy using effective Ru-photosensitizers for glioblastoma.

We report here synthesis, characterization and crystal structures, solvation kinetics, and binding studies with CT-DNA and HSA. The photoactivity in the low energy UV-A light (λ_{exc} = 365 nm) was investigated for possible phototherapeutic applications. The *in vitro* MTT-based cytotoxicity studies with glioblastoma (GB) cell line LN229 and normal fibroblast cell line L929 showed both the complexes are significantly potent with a better selectivity index (S. I.) for compound **1**. The therapeutic potency of complex **1** further shows ~75% inhibition of clonogenic potential and lower the migratory potential as revealed from the wound healing assay. The apoptotic cell death pathway is evident from the nuclear localization, condensation, and blebbing and increased caspase 3/7 activity.

Result and Discussion

Physiochemical characterizations.

The Schiff base ligands were synthesized in high yields from 3-aminoquinoline with 2-hydroxy benzaldehye (L1) or 2-hydroxy-1-naphthaldehye (L2) via refluxing in EtOH. [Ru(η^6-*p*-cymene)(L1)Cl] (**1**) and [Ru(η^6-*p*-cymene)(L2)Cl] (**2**) complexes were synthesized in high yields via stoichiometric reaction of respective deprotonated ligand with dimeric [Ru(η^6–*p*-cym)(μ-Cl)Cl]$_2$ in $CHCl_3$ at 50 ^{0}C for 4 h. Complexes were non-hygroscopic crystalline solids and soluble in CH_2Cl_2, $CHCl_3$, MeOH, CH_3CN, DMF and DMSO and insoluble in H_2O, Et_2O and pentane/hexane. Both the complexes were well characterized using ESI-MS, FTIR, NMR, and UV-vis studies. The solid-state structures of both the complexes was determined using single-crystal X-ray diffraction studies showing the typical three-legged piano-stool structure. Selected spectral data are given in Table 1.

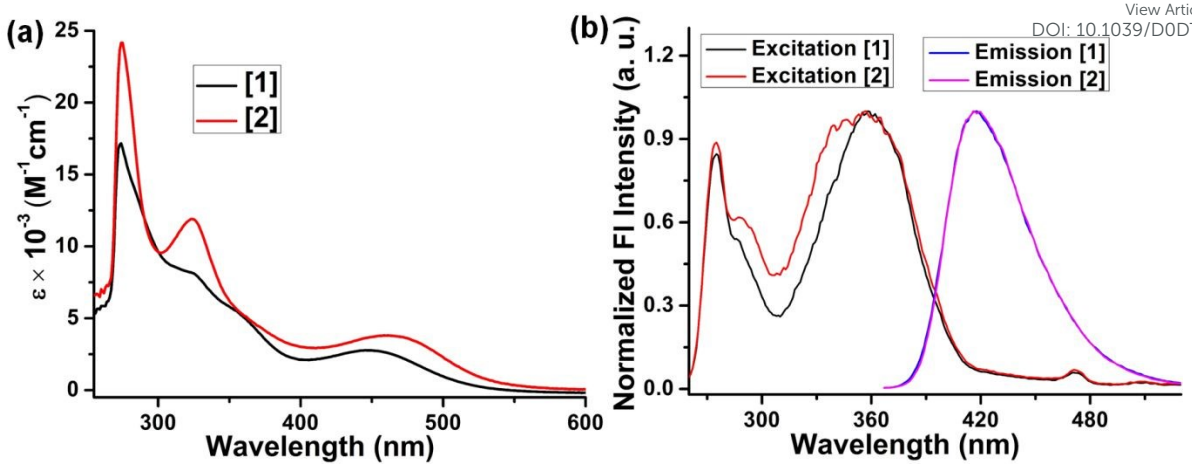

Fig. 3 (a) Electronic absorption spectra of complexes **1** and **2** in DMF (C = 39 μM) at 298 K. (b) An overlay of the excitation and emission spectra of the complexes **1** and **2** in DMF (C = 20 μM) at 298 K. Excitation parameters: λ_{em} = 550 nm and exc. and em. slit width = 10 nm. Emission parameters: λ_{ex} = 355 nm and exc. and em. slit width = 5 nm.

The (+)-ve mode ESI-MS analysis of the complexes in $CHCl_3$ showed molecular ion peaks corresponding to $[M–Cl^-]^+$ at m/z for 483.10 (**1**) and 533.12 (**2**) arising from the dissociation of the chloride with characteristic isotopic patterns of Ru (Fig. S1, ESI†). The FT-IR spectra of the complexes displayed a series of strong stretching peaks ranging 1606–1443 cm^{-1} (**1**) and 1616–1429 cm^{-1} (**2**) corresponding to $\nu_{C=C}$ and $\nu_{C=N}$ functionalities of the ligands [18]. The absence of any broad band at ~3300 cm^{-1} typical for $\nu_{O\text{-}H,}$ which confirms the deprotonated Schiff-base metal coordination (Ru^{II}-OPh) (Fig. S2, ESI†). [19]. Further, the structural integrity of the complexes in solution was determined by ^{1}H-NMR and ^{13}C-NMR (Fig. S3−S6, ESI†). and chemical shift values are assigned in experimental sections. The absence of ^{1}H NMR signals corresponding to –OH group also confirms Ru^{II}-OPh coordination. The $–CH_3$ (s, 3H) of *p*-cymene resonated at 2.14 (**1**) and 2.17 (**2**) ppm. A septate signal corresponding to -CH-$(CH_3)_2$ of *p*-cymene was observed at 2.63 (**1**) and 2.64 ppm (**2**). The electronic absorption spectra showed three maxima (λ_{max}) bands for **1** at 274 nm, 325 nm and 447 nm, and for complex **2** at 275 nm, 323 nm and 461 nm (Fig. 3 (a), Table 1). The highest energy band corresponds to π–π* of ligands (L1 and L2), while lowest energy visible region bands corresponds MLCT transitions, whereas the bands ~ 325 nm for both the complexes are probably due to n–π* transitions [20]. The complexes were fluorescent and showed identical emission maximum at 417 nm when excited at 355 nm in DMF solution (Fig. 3b). The excitation from lowest energy band (λ_{ex} = 447 nm (**1**) and λ_{ex} = 461 nm (**2**)) showed very weak emission at 560 nm (**1**) and 532 nm (**2**). The excitation spectra displayed bands at 275 nm, 288

nm, and 357 nm (λ_{em} = 550 nm) in DMF and show features from absorption spectral pattern (Fig. 3(b)).

Table 1. Physiochemical parameters of the complexes **1** and **2**.

Complex	IR[a]/cm^{-1}, $\nu_{C=C,}$ $\nu_{C=N}$	λ_{max}[b]/nm, (ε/M^{-1}cm^{-1})
1	1606, 1527, 1492, 1459, 1443	274 (16300), 325 (7800), 447 (2780)
2	1616, 1603, 1581, 1535, 1453, 1429	275 (23750), 323 (11220), 461 (3810)

[a]in KBr phase. [b]UV-visible spectra in DMF.

Single crystal X-ray structure

Both the complexes Ru(η^6-*p*-cymene)(L1)Cl] (**1**) and [Ru(η^6-*p*-cymene)(L2)Cl] (**2**) and ligand 2-[(*E*)-(3-quinolinylimino)methyl)naphthol (L2) were crystallized at ambient conditions and structures were determined by single-crystal X-ray diffraction studies. The ORTEP view of **1**, **2,** and L2 was shown in Fig. 4 and Fig. S7(a), respectively. The crystallographic parameters are noted in Table S1, and selected bond parameters are given in Table S2 in ESI†. The unit cell of L2 and complexes **1** and **2** contain 8, 8 and 4 molecules respectively (Fig. S7(b) and Fig. S8 in ESI†). Complex **1** and L2 crystallized in monoclinic *C2*/*c* and complex **2** in $P2_1/c$ space groups. The free ligand L2 shows minor deviation from the coplanarity between quinoline and naphthol rings, and displayed ideal cisodial orientation of imine-N and phenolic-OH group for coordination with Ru^{II} centre (Fig. S7, ESI†). The coordination environment around the Ru(II) centre found identical (distorted octahedral) with a tetrahedral like geometry from (η^6- *p*-cymene) capping one vertex, the chelating *N*,*O* bidentate Schiff-bases and monodentate chloride, making an overall "piano stool" geometry typical for Ru(II)-arene complexes [21,22]. The Ru^{II}-η^6-cymene (centroid) distances are ~1.67 Å (**1, 2**). The Ru-N bond distances are 2.097(4) Å (**1**) and 2.096(3) Å (**2**). The shortest and largest bonds are Ru-O (2.078(3) Å for **1** and 2.059(2) Å for **2**) and Ru-Cl (2.4285(10) Å for **1** and 2.4243(9) Å for **2**) matching with the reported Ru^{II}-arene complexes [23−25]. The shorter bond lengths in complex **2** than **1** for the Ru-N1/O1/Cl1 bonds suggest more π–acceptor ability of L2 through extended conjugation in complex **2**. The dihedral angle between the quinoline ring and phenyl/naphthyl groups are 20.06° (L2), 48.04° (**1**), and 42.99° (**2**) indicates significant twisting of ligand planarity upon binding to Ru^{II}-(η^6-cym) moiety (Fig. S9 in ESI†). Both the complexes **1** and **2** show weak intermolecular π–π stacking interactions among planar aromatic rings at 3.575 Å and 3.504 Å, respectively (Fig. S10 in ESI†).

View Article Online
DOI: 10.1039/D0DT02167A

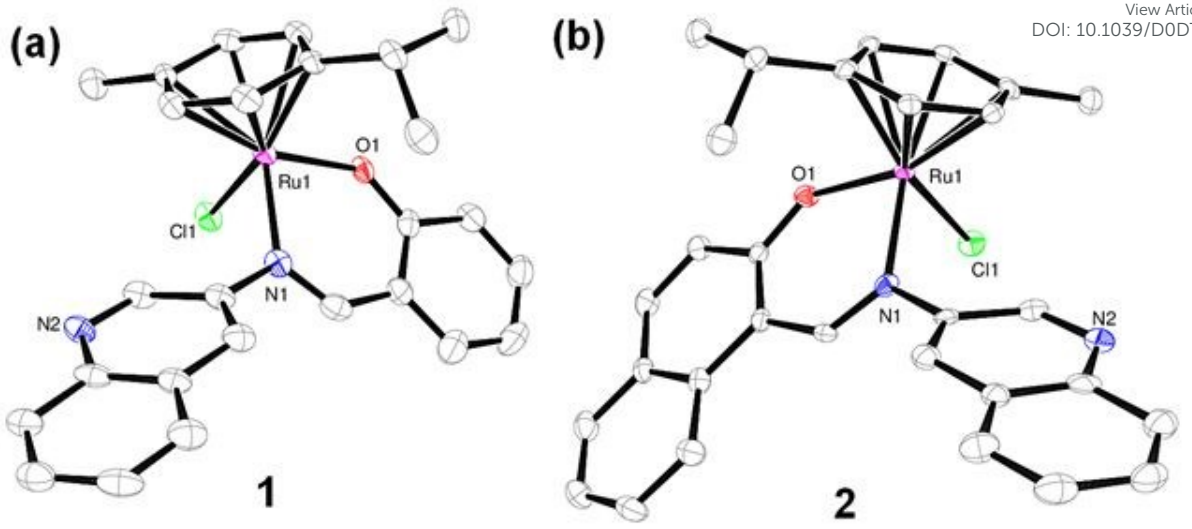

Fig. 4 ORTEP views of **1** and **2** with 50% probability of thermal ellipsoid and labelling of metal and heteroatoms. (a) Ru(η^6-*p*-cymene)(L1)Cl] (**1**) (CCDC 2006007): Ru1-N1, 2.097(4) Å; Ru1-O1, 2.078(3) Å; Ru1-Cl1, 2.4285(10) Å. (b) [Ru(η^6-*p*-cymene)(L2)Cl] (**2**) (CCDC 2006008): Ru1-N1, 2.096(3) Å; Ru1-O1, 2.059(2) Å; Ru1-Cl1, 2.4243(9) Å. The hydrogen atoms were not shown for clarity.

Solvation of Complexes

The hydrolysis or aquation is the key step of the activation of several metal-based chemotherapeutics. A majority of the metallodrugs (e.g., platins) are truly based on tuneable and variable ligand exchange rates with H_2O [26, 27]. All the notable Ru-drugs (NAMI-A, NKP1339, RM175, RAPTA-C) contain Ru-Cl bonds with anticipation of ligand exchange reaction from a potential donor from biological targets. The labile Ru–Cl bonds undergoes hydrolysis and forms Ru–OH_2 bond, and the later can bind to DNA nucleobases (guanine N7 and adenine) by substitution of labile water. In general, the rate of hydrolysis of monofunctional Ru(II)-arene complexes (containing labile ligands such as halides) correlated with their cytotoxicity and pharmacokinetics profile. The inert Ru-complexes remain inactive while moderate hydrolysis exhibits pronounced targeted cytotoxicity. Further, the rate of hydrolysis is tuneable and depends on the substituent present on the arene ring, and other secondary ligands attached to Ru(II) [28−30].

The solvation or aquation of the complexes **1** and **2** was studied in 5 mM Tris-HCl/NaCl buffer (pH = 7.2), as well in DMF from the time-dependent UV-visible and fluorescence spectral measurements at 298 K due to their well-defined spectroscopic signatures. The UV-vis spectra

View Article Online
DOI: 10.1039/D0DT02167A

of complex **1** and **2** dissolved in aqueous buffer showed concomitant small increase in absorbance at 395 nm (**1**) and 379 nm (**2**) (Fig. 5(a) and Fig. S11(a)). The insignificant absorption spectral changes indicate possible aquation reaction (Ru-Cl→Ru-OH_2) without any major electronic or structural perturbation affecting the chromophoric ligands bound to Ru(II). The rate constants (k_{H2O}) for these hydrolysis reactions were determined using these bands (Fig. 5(b) and Fig. S11(b)). The rate constants of hydrolysis (k_{H2O}) and half-life time ($t_{1/2}$) of the complexes were obtained from the first-order exponential curve fitting by following equation (1) (Table 2). The concomitant changes in absorption spectra in DMF and the rate constants of solvation in DMF (k_{DMF}) and half-life ($t_{1/2}$) were obtained by monitoring maximum change in absorbance at 325 nm (**1**) and 324 nm (**2**) in DMF (Table 2, Fig. S12, ESI†)

Table 2. Solvation kinetics parameters of the complexes **1** and **2** at 298 K.

Complex	Aquation (H_2O)		Solvation (DMF)	
	[a]k_{H2O} (s^{-1})	[b]$t_{1/2}$ (min)	[c]k_{DMF} (s^{-1})	[d]$t_{1/2}$ (min)
1	5.58×10^{-4}	20.7	4.13×10^{-4}	28.0
2	8.47×10^{-5}	136.4	3.67×10^{-4}	31.5

[a]Hydrolysis rate constant in 5 mM Tris-HCl/NaCl buffer (pH = 7.2), [b]Half-life time of hydrolysis, [c]Solvation rate constant in DMF, [d]Half-life of solvation.

The differences in solvation rate constants for the complex **1** than **2** can be accounted from better π-acceptor ability of complex **2** from extended aromatic conjugations in L2, which decreases the electron density and lability around Ru(II) $4d^6$ centre [31]. The rate of hydrolysis of complex **1** is faster than cisplatin, which exhibits hydrolysis rates of 7.56×10^{-5} and 6.32×10^{-5} s^{-1} for the first and second chloride ligands [32].

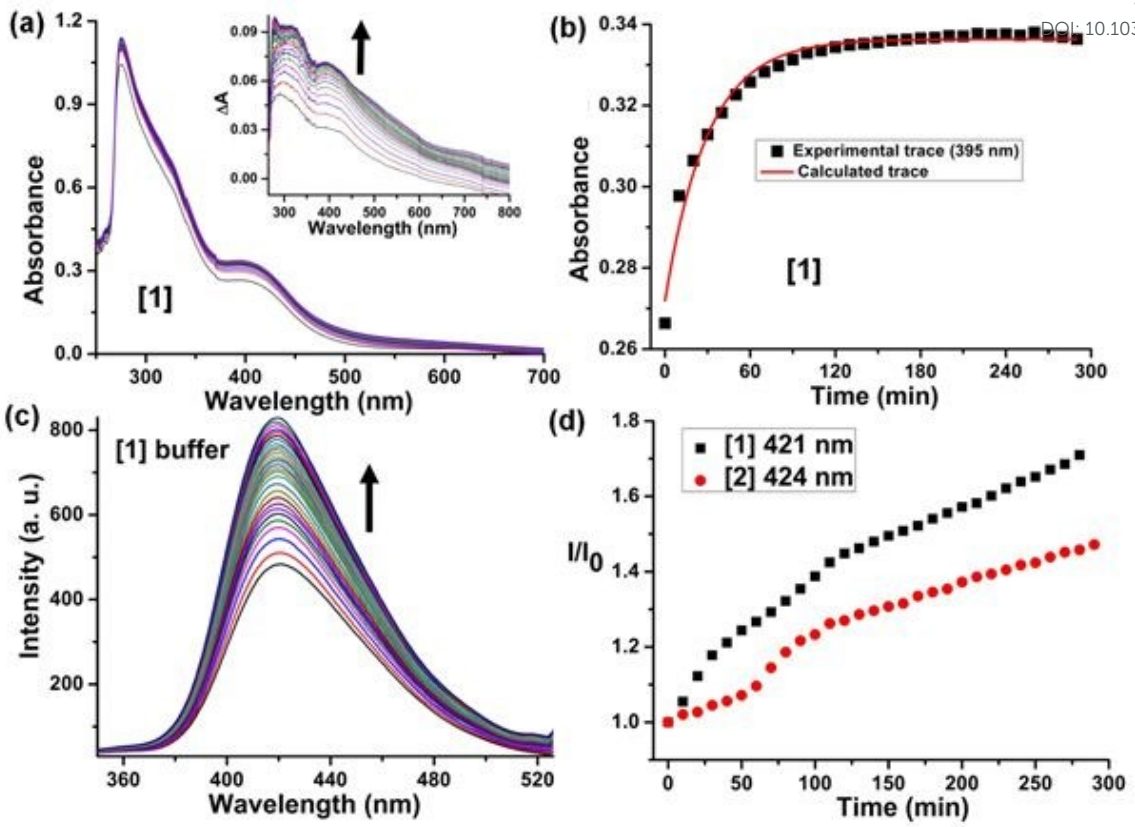

Fig. 5 (a) The changes in absorption spectral profile for the complex **1** (58 μM) in 5 mM Tris-HCl/NaCl buffer (pH = 7.2)-DMF mixture (97:3). Inset: Evolution of UV-visible difference spectra upon aquation of complex **1**. (b) Absorption traces at 395 nm and monoexponential fit upon hydrolysis for complex **1**. **(**c) The changes in fluorescence spectral profile for the complex **1** (10 μM) in 5 mM Tris-HCl/NaCl buffer (pH = 7.2)-DMF mixture (200:1) (d) Increase of emission intensity at 421 nm (**1**) and 424 nm (**2**) for the complexes upon hydrolysis in 5 mM Tris-HCl/NaCl buffer (pH 7.2). λ_{exc} = 275 nm, Ex. and Em. slit width = 10 nm at 298 K.

The hydrolysis of the complexes further evaluated from fluorescence measurement in buffer at 298 K, which showed concomitant increase of emission intensity at 421 nm (**1**) and 424 nm (**2**) (Fig. 5(c), (d) and Fig. S13, ESI†). The enhancement in emission intensity for complex **1** was more pronounced than complex **2** in agreement with a faster rate of hydrolysis of complex **1** as observed from absorption spectral measurements. The aquated products apparently exhibit higher emission intensity than the original complexes. This can be probably from the heavy atom displacement (Cl) by H_2O; the former facilitates the triplet-state population and thereby decrease in fluorescence intensity [33].

Photoreactivity

The Ru(II)-polypyridyl complexes having excellent photoreactivity due to rich photochemistry mediated by energy transfer from photogenerated triplet ^{3}MLCT excited to low-lying triplet metal-centered (^{3}MC) excited states [34]. The Ru(II)-arene complexes containing secondary aromatic chromophores can be potentially photoactivated to undergo ligand dissociation or de-arenation reactions. These photo-substituted Ru-products sometime are avid binder of DNA, or capable of generating ROS for PDT [35, 36]. In addition, light activation of Ru(II) complexes selectively trigger the release of Ru-bound bioactive ligands/drugs for feasible PACT [37, 38].

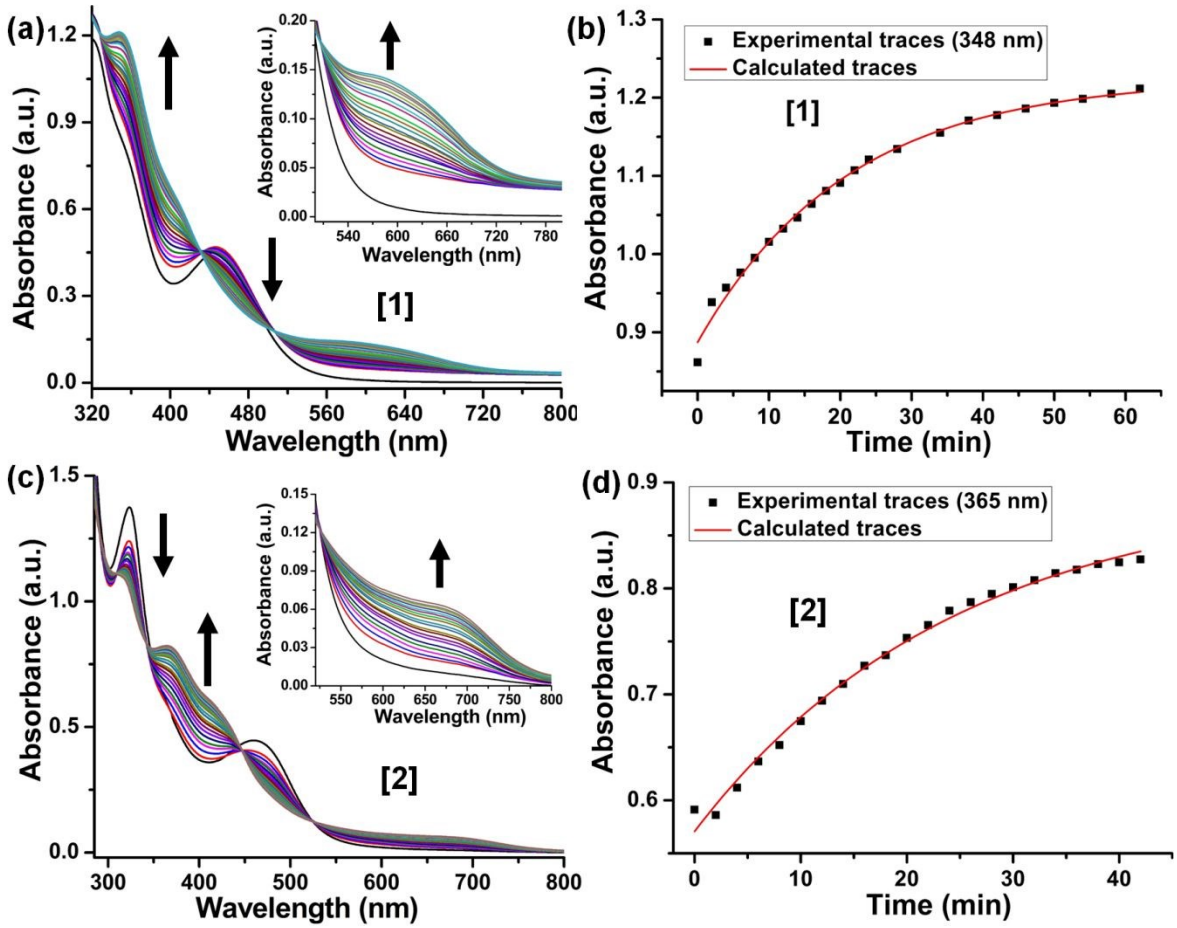

Fig. 6 The photo-irradiation of UV-A light of 365 nm (6 W) to the complexes at 298 K. (a) **1** (11 μM) for 0–62 min and (c) **2** (8 μM) for 0–42 min resulted in alteration in electronic absorption spectra. (b) The evolution of $A_{348\ nm}$ absorption band for complex **1** as a function of photo-exposure time with monoexponential fitting. (d) The variation of $A_{365\ nm}$ absorption band for complex **2** with photo-exposure time with monoexponential fitting. Inset (a) and (c) show the evolution of a new absorption band in the range of 500–800 nm (**1**) and 520–800 nm (**2**), respectively.

The photo-irradiation of both the complexes in DMF solution with low power UV-A light of 365 nm (6 W) at RT resulted in concomitant changes of absorption bands (Fig. 6). The complex **1** showed the formation of a new band at 348 nm, along with and a broad band at ~580 nm (Fig. 5(a) and inset). The band of 447 nm disappears over the photo-exposure time with the evolution of isosbestic points at 330, 432 and 505 nm, indicating the formation of a single photoproduct. Similarly, the complex **2** showed a decrease in intensity at 323 nm, and the disappearance of 461 nm band with simultaneous evolution of a new band at 365 nm. The photoirradiation also resulted in the appearance of a new low-energy band in the range of 500-800 nm with λ_{max}~ 675 nm (Fig. 6(c) and inset). The photo illumination resulted in clear isosbestic points at 310, 343, 448, and 525 nm suggesting unique photochemical product formation. The changes in A_{348} (**1**) and A_{365} (**2**) were used to calculate the kinetic parameters. The calculation suggested the half lifetime ($t_{1/2}$) 14.5 min (**1**) and 17.0 min (**2**), and the first-order rate constants (7.96±0.46) × 10^{-4} and (6.79±0.59) × 10^{-4} s^{-1} for complex **1** and **2** respectively (Fig. 6(b), (d) and Table S3, ESI†). These significant changes in absorption possibly arising from the arene-loss and/or formation of solvated species with potential PACT application, as reported for several Ru(II)-arene complexes [39].

CT-DNA Binding

DNA is the most explored biological target for the anticancer agents, especially platins and many Ru(II) compounds [40]. The monofunctional organoruthenium complexes are known for binding of double helical DNA with guanine N-7 site selectivity [41]. The double helical architecture of DNA consisting of nucleobases linked with phosphate-deoxyribose chains exhibit a variety of interactions: non-covalent (H-bonding and π–π interactions), covalent (cross-linking and adduct formation) and electrostatic interactions. These interactions lead to structural perturbations of DNA and ultimately resulted in inhibition of the replication processes, thus binding efficacy of metallodrugs with DNA correlated with the potential of complexes to damage cancer cells.

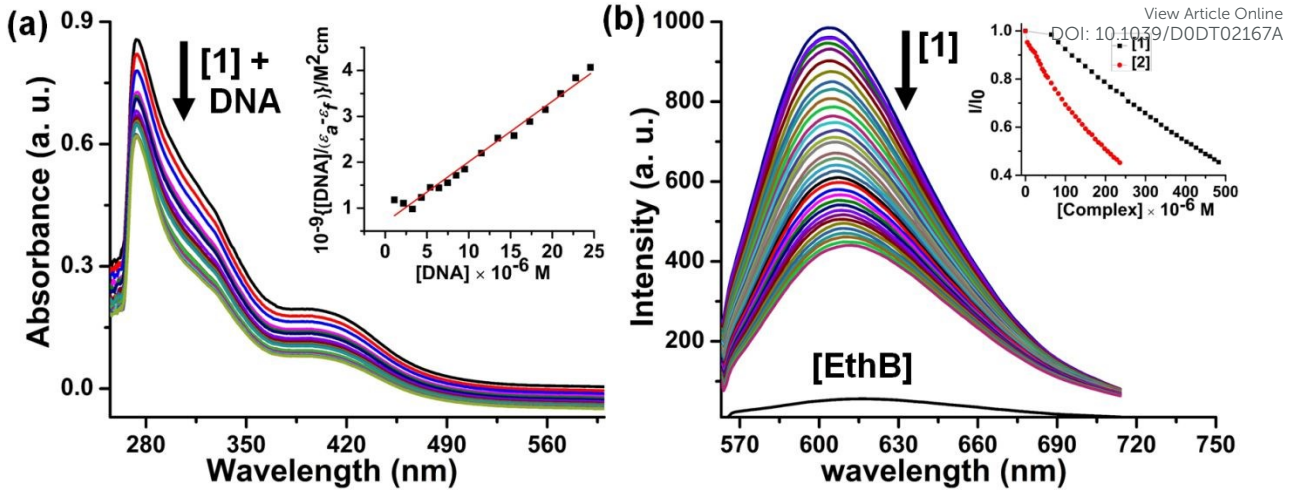

Fig. 7 The binding propensity of the complexes **1** and **2** with CT-DNA. (a) The continuous decrease of absorbance of complex **1** (39 μM) upon gradual addition of CT-DNA (0–25 μM) in 5 mM Tris-HCl/NaCl buffer (pH = 7.2)-DMF mixture (50:1). Inset: Determination of binding constant (K_b) of complex **1** with CT-DNA from the slope to intercept ratio of the linear fitted plot of [DNA] vs. DNA/ε_a-ε_f from equation (2). (b) The decrease of emission intensity of EthB (12.5 μM) bound CT-DNA upon addition of complex **1** (0–483 μM), λ_{ex} = 546 nm, Ex and Em slit width = 10 nm. Inset: An overlay of the variation of I/I_0 (604 nm) vs. [Complex].

The absorption spectral studies provided information about binding affinity and showed significant hypochromic shifts due to π–π interactions and bathochromic shifts upon stabilization of duplex DNA [42]. The gradual addition of CT-DNA at constant complex concentration lead to a significant decrease in absorbance of π–π* and MLCT bands of the complexes (Fig. 7a and Fig. S14, ESI†) The results indicate possible non-covalent interactions between the complex and DNA. The intrinsic DNA binding constants (K_b) calculated from equation (2) (Table 3).

Table 3. The binding parameters for the complexes **1** and **2** with CT-DNA and HSA

Complex	[a]K_b	[b]K_{app}	[c]C_{50}	[d]K_{HSA}	[e]K_q	[f]K	[g]n
1	1.91×10^5	3.30×10^5	378	3.75×10^5	3.75×10^{13}	6.12×10^5	1.04
2	5.32×10^5	6.07×10^5	206	3.01×10^5	3.01×10^{13}	8.74×10^4	0.91

[a]K_b, Intrinsic binding constant with CT-DNA. [b]K_{app}, apparent binding constant with CT-DNA. [c]C_{50}, the complex concentration (μM) corresponding to the 50% decrease of emission intensity of EthB-DNA adduct. [d]K_{HSA}, Stern-Volmer quenching constant of fluorescence for HSA. [e]K_q, Quenching rate constant. [f]K, HSA binding constant of complexes. [g]n, number of binding sites.

Further, to get more insight of the possible intercalation of complexes to DNA, ethidium bromide (EthB) displacment assay was performed. The efficient quenching by aqueous buffer makes EthB weakly emissive, and in the presence of DNA showed enhanced fluorescence intensity [43]. The fluorescence emission of EthB-DNA adduct upon addition of complexes **1** and **2** showed a significant decrease of intensity at 604 nm (Fig. 7b and Fig. S15 ESI†). The spectral changes correspond to the displacement of EthB from its DNA adduct. The competitive binding of complexes to DNA determined from their apparent binding constants (K_{app}) (Table 3).

The complexes were further studied using circular dichroism (CD) spectral titration for their ability to perturb helicity of chiral ds-DNA structure from. The results showed that the complexes results in minimal structural perturbation of DNA double-helix (Fig. S16, ESI†).

Human Serum Albumin (HSA) binding

Human serum albumin (HSA), being the most abundant protein in blood plasma, plays a crucial role in numerous physiological processes-regulation of osmotic pressure and pH, and transportation of endogenous metabolites. Serum proteins expresses affinity towards drugs and other toxicants, and thereofore capable of modulating their action or delivery [44, 45]. The optimum drug binding affinity of HSA is of significant concern for therapeutic effect and drug development. The single tryptophan residue in domain IIA (Trp-214) is responsible for the fluorescence of the HSA and highly sensitive to the microenvironment and thus serves as a spectral probe for the ligand binding [46].

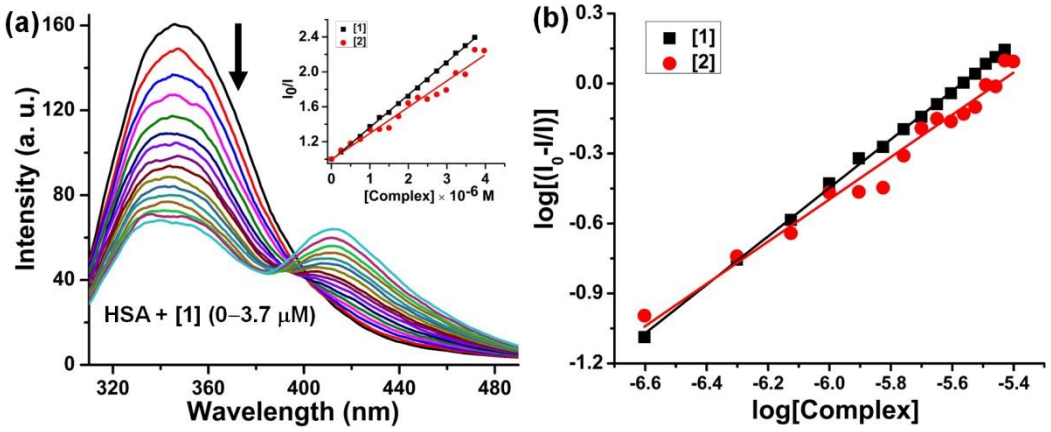

Fig. 8 (a) The changes in emission intensity of HSA with increasing concentration complex **1** (0–3.7 μM) in 0.8% DMF-5 mM Tris-HCl/NaCl buffer (pH 7.2) mixture, λ_{exc} = 295 nm, λ_{em} = 346 nm, slit 10/5 nm. Inset: An overlay of Stern-Volmer quenching plot for the complexes **1** and **2**. (b) An overlay of log [Complex] *vs*. log $[(I_0\text{-}I)/I]$ for the complexes **1** and **2**.

The lead Ru(III) antimetastatic agent NAMI-A and anticancer agent KP1019 show a higher binding affinity to HSA and structurally well characterized [47−49]. The half sandwich ruthenium-arene complexes can covalently bind to the amino acid residues of HSA and could even induce oxidation of cysteine thiolate (Cys-34) to sulfinate [50].

The interaction of complexes **1** and **2** with HSA was studied from fluorescence quenching measurements. The addition of complexes **1** and **2** to the HSA resulted in a significant decrease in protein fluorescence with no shift of λ_{em} indicating the retention of the overall polarity of HSA (Fig. 8a and Fig. S17 ESI†). The second emission peak at $\lambda_{em} \sim 413$ nm originated from intrinsic emission of complex **1** upon binding to a hydrophobic pocket of HSA. The quenching of emission may originate from the numerous supramolecular interactions; excited-state and/or ground-state complex formation, collisional quenching, and ligand-induced conformational changes [51].

The Stern-Volmer quenching constant (K_{HSA}) and Stern-Volmer quenching rate constants were determined from equation (3) and equation (4) respectively (Table 3). The HSA binding constant for the complexes (K) and the number of sites (n) available was measured from the modified Stern-Volmer equation (5), suggesting a moderate binding affinity to HSA at single binding site.

Conformational analysis from synchronous fluorescence

In a multichromophoric system, the synchronous fluorescence spectra can provide information about the microenvironment of specific residue. The spectral advantages over fluorescence are the spectral simplifications, reduced bandwidth, and retained sensitivity of fluorescence. The technique utilizes a simultaneous scanning of excitation and emission monochromators by keeping fixed wavelength differences ($\Delta\lambda$) between them. The $\Delta\lambda$ = 15 nm and $\Delta\lambda$ = 60 nm signifies the molecular microenvironment of tyrosine and tryptophan residue of HSA respectively [52].

The synchronous fluorescence spectral measurement with $\Delta\lambda$ = 15 nm and $\Delta\lambda$ = 60 nm for HSA upon addition of complexes **1** and **2** resulted in the significant quenching of emission at 284 nm [(% I/I_0 = 67 (**1**) and 66 (**2**)) 279 nm (% I/I_0 = 43 (**1**) and 44 (**2**)] respectively (Fig. 9 and Fig. S18). These results indicate the tryptophan as preferential binding site for the from both the complexes.

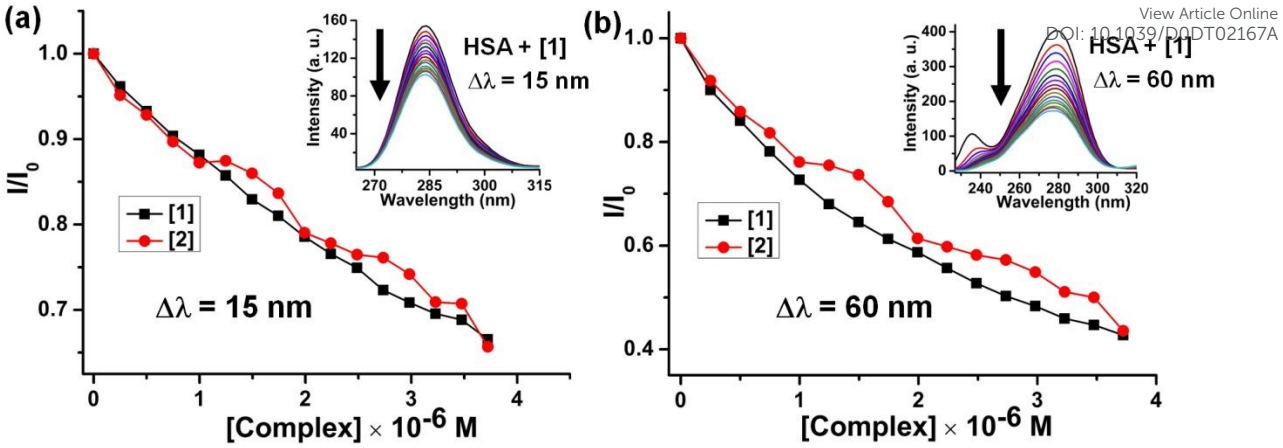

Fig. 9 The synchronous fluorescence measurement of HSA (2.4 μM) upon addition of complexes (0–3.7 μM) **1** and **2** in 0.8% DMF-5 mM Tris-HCl/NaCl buffer (pH 7.2) mixture at 298 K. (a) Overlay of I/I_0 at 284 nm vs. [complex] for $\Delta\lambda$ = 15 nm, inset: Spectral traces of the HSA upon titration with complex **1**. (b) Overlay of I/I_0 at 279 nm vs [complex] for $\Delta\lambda$ = 60 nm, inset: Spectral traces of the HSA upon titration with complex **1**. Slit width for exc./em. = 10/5 nm.

Cellular Studies: *In vitro* cytotoxicity

The cytotoxic effects of both the complexes **1** and **2** along with *cis*platin, a well-known metallodrug, have been studied by MTT assay in the human brain GB cell line LN229. The cytotoxicity was also compared with normal mouse fibroblast subcutaneous cell line L929. Each compound was tested at a minimum of six concentrations, and the IC_{50} value was determined from the dose-response curves (Fig. 10). While both the Ru-complexes showed similar cytotoxicity in the GB LN229 cell line (Fig. 10a); however, the complex **2** exhibited much higher cytotoxicity towards normal fibroblast cells than **1** (Fig. 10b).

Table 4. IC_{50} values and selectivity index (S.I.) of complexes **1** and **2** with GB LN229 and normal mouse fibroblast L929 cells.

Complexes	**1**		**2**	
Cell lines	**IC_{50} (μM)[a]**	**S.I.[b]**	**IC_{50} (μM)[a]**	**S.I.[b]**
LN229	22.8 ± 1.5	3.0	21.7 ± 1.5	2.0
L929	68.5 ± 0.7	-	44.0 ± 0.3	-

[a]Concentrations in μM determined for complexes after 24 h incubation.
[b]Selectivity index (S.I.) for complexes measured after 24 h incubation, see the experimental section for detail.

View Article Online
DOI: 10.1039/D0DT02167A

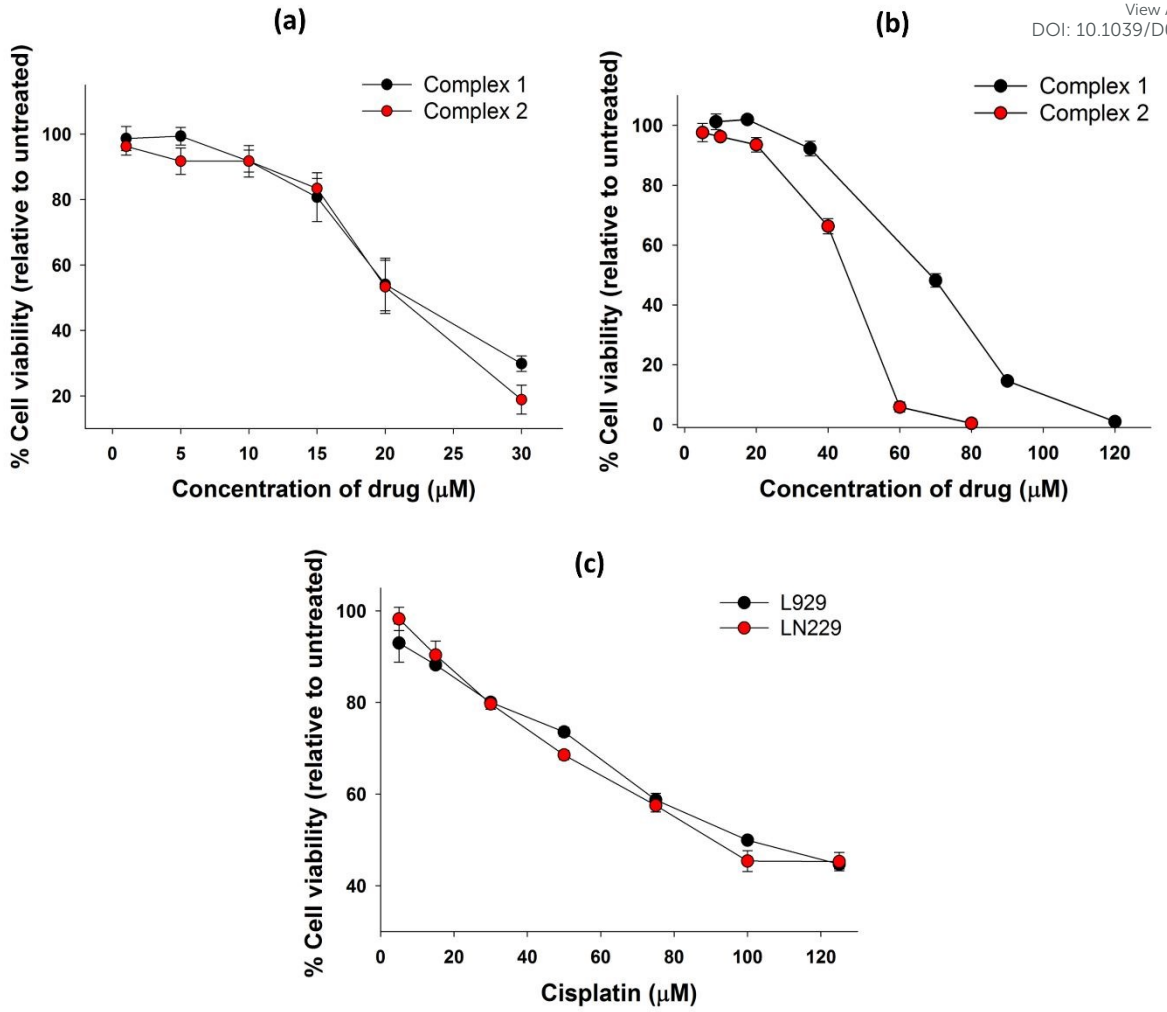

Fig. 10 Dose-dependent cytotoxicity of the complexes **1** and **2** and *cis*platin: (a) LN229 GB cell line, (b) L929 fibroblast cell line, (c) *cis*platin in both LN229 and L929. Data are expressed as the mean (± SD) for three independent experiments.

The % cell viability was used to calculate the selectivity index (S.I.), the parameter indicating selectivity of a drug towards cancer cells compared to normal cells, was determined according to equation (7). [Ru(η^6-*p*-cymene)(L1)Cl] (**1**) was found more selective towards GB cells (S. I. = 3), while [Ru(η^6-*p*-cymene)(L2)Cl] (**2**) displayed moderate selectivity (S. I. = 2) (Table 4). Both the complexes exhibit higher cytotoxicity than *cis*platin for the GB cells (Fig. 10c). From the dose-survival curve, it is evident that *cis*platin has a poor selectivity towards cancer cells, and indiscriminately kills normal cells equally well; probably indicating its well-known side effects (Fig. 10c). Due to better efficacy and selectivity, further detailed anticancer studies were carried out with complex **1**.

Effect on cellular proliferation

The effect on cellular proliferation over a prolonged time was investigated by incubating GB LN229 cells with [Ru(η^6-*p*-cymene)(L1)Cl] (**1**) at its IC_{50} concentration (22.8 μM) and monitoring cell viability at various time periods by MTT cell viability assay. It was observed that complex **1** significantly inhibits the proliferation of LN229 GB cells (Fig. 11).

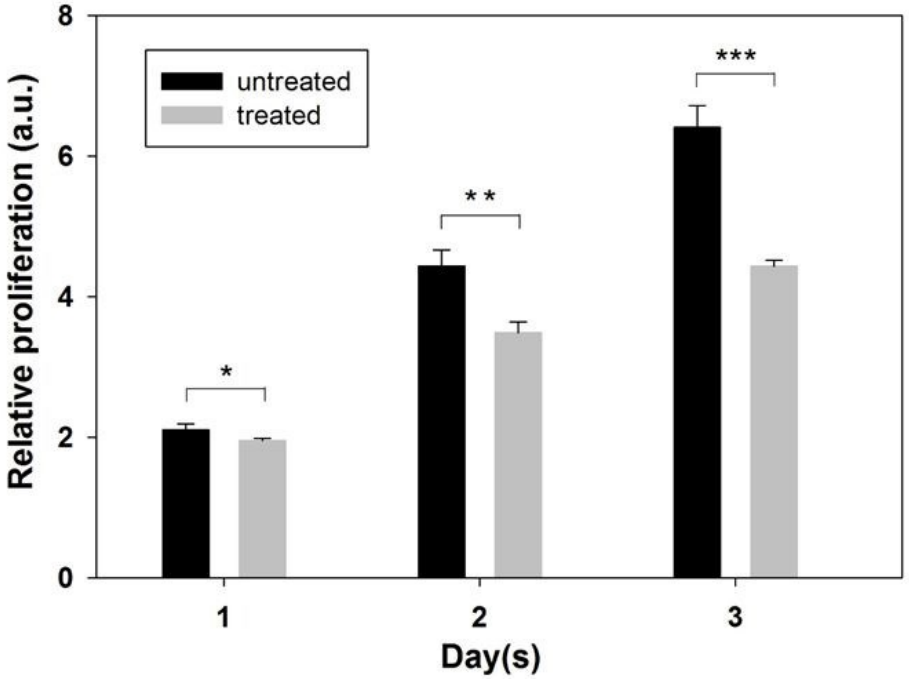

Fig. 11 The complex **1** at its IC_{50} concentration inhibits the proliferation of LN229 cells as detected by MTT cell proliferation assay. The graphical data points represent mean ± SD of at least three independent experiments (*p > 0.01 and <0.05, **p < 0.01, ***p < 0.001). Error bars denote ± SD.

The clonogenic potential is the ability to proliferate into multiple cells from a single cell; it also gives an effective measure of cellular proliferation. The ability to form a colony of cells from a single cell was measured for both untreated and complex **1** treated cells using the colony formation assay. Interestingly, colony formation was significantly inhibited in complex **1** treated cells. Both the number of colonies and their sizes were diminished significantly (~75%) in the latter group of cells (Fig. 12).

View Article Online
DOI: 10.1039/D0DT02167A

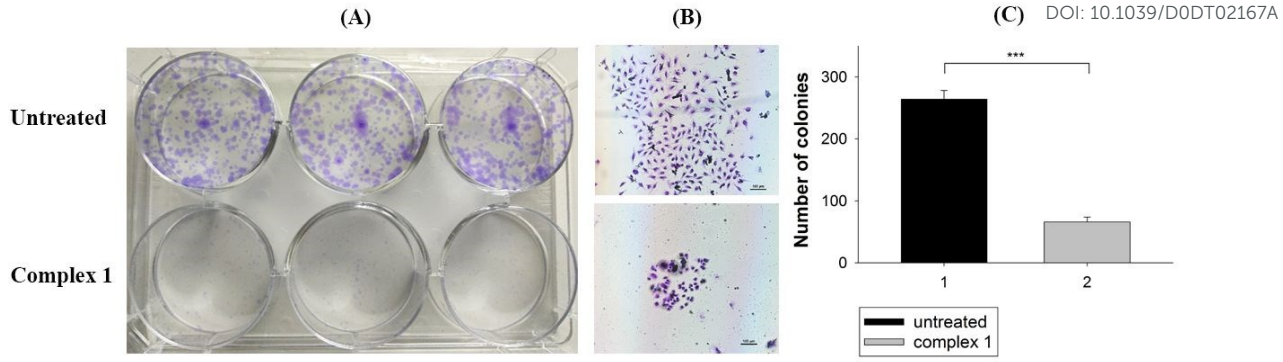

Fig. 12 LN229 cells treated with complex **1** (22.8 μM) show poor clonogenic potential as determined by the colony formation assay: (A) A six well plate displaying colonies formed in untretaed and Complex **1** treated cells, (B) microscopic images of formed colonies, (C) quantitative estimation of number of colonies formed. The graphical data points represent mean ± SD of three independent experiments. Error bars denote ± SD.

Effect on cellular migration

The antimetastatic property of Ru-complexes (e.g., NAMI-A, RAPTA-C) are uniquely advantageous along with their cytotoxicity [53]. Enhanced cellular migration is a crucial property of cancer cells that contributes to rapid tumor progression and metastasis. To evaluate whether complex [Ru(η^6-*p*-cymene)(L1)Cl] (**1**) has any effect on migration of GB cells, the *in vitro* scratch assay or wound healing assay was performed. A scratch wound was created in the monolayer of LN229 cells, and the cells were incubated with serum-free media with/without complex **1**. It was observed that the cells treated with complex **1**, had significantly lower migratory potential as compared to the untreated control group of cells (Fig. 13). The results show that complex **1** effectively restrain the migratory potential of GB cells.

View Article Online
DOI: 10.1039/D0DT02167A

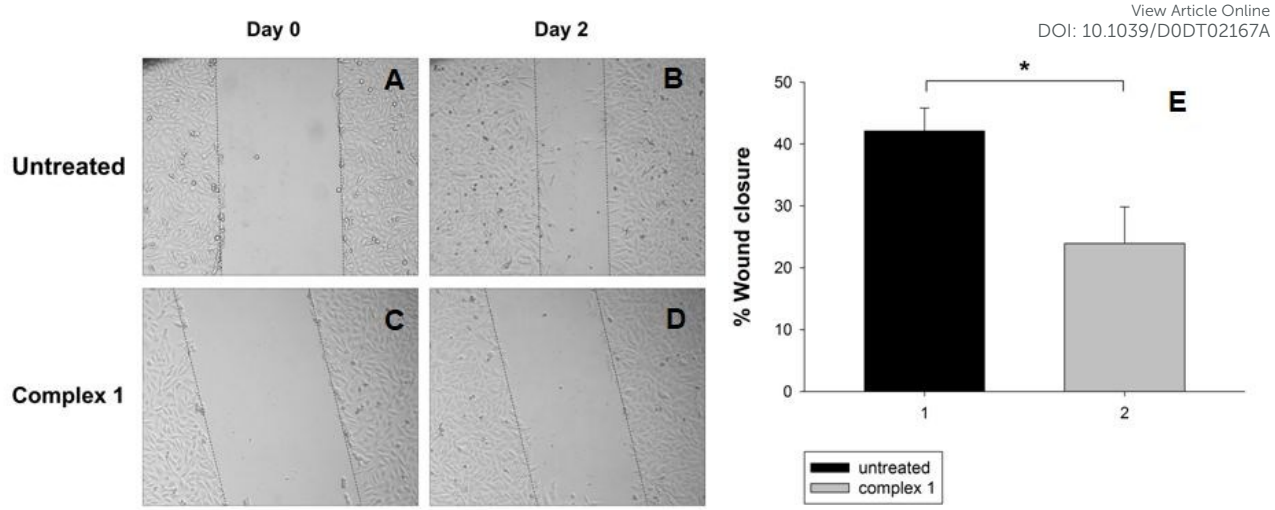

Fig. 13 Migration inhibition of glioblastoma LN229 cells in presence of complex **1** (22.8 μM) as detected by in vitro scratch assay. (A) and (B) represent the migration of untreated cells on day 0 and day 2 respectively; while (C) and (D) represent the same for complex **1** treated cells; E is a quantitative representation of relative migration between untreated and treated cells. The graphical data points represent mean ± SD of two independent experiments. Error bars denote ± SD.

Apoptosis assessment

To check whether complex **1** imparts anti-GB activity by inducing apoptosis, we incubated the GB LN229 cells with complex **1** for 48 hours and performed DAPI nuclear staining to detect any morphological changes using fluorescence microscopy. Furthermore, the highly sensitive Caspase-Glo® 3/7 luminescent assay was used to measure caspase-3/7 activities as a genuine marker for apoptotic cell death [54]. As demonstrated in Fig. 14B and D, the cells treated with complex **1** showed the characteristics of apoptotic nuclei morphology, i.e. fragmented and condensed DNA with nuclear blebbing, while the untreated cells (Fig. 14A and C) maintained smooth and round contours, which are characteristic of healthy nuclei.

The results from the DAPI staining experiment was further validated with the caspase 3/7 assay. We observed ~64% increase in the caspase 3/7 activity in cells treated with complex **1** when compared to the untreated control (Fig. 14D). Caspase activation indicates the onset of the cellular apoptotic pathways in LN229 cells in the presence of the complex **1**.

View Article Online
DOI: 10.1039/D0DT02167A

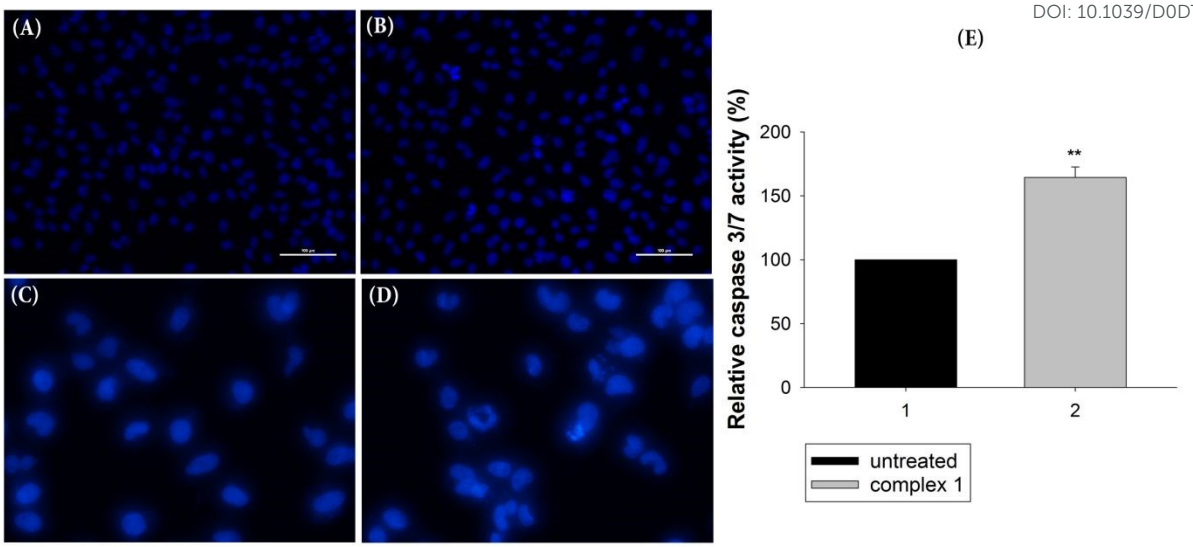

Fig. 14 The effect of complex **1** (22.8 μM) on apoptosis. Representative photomicrographs showing nuclear morphology of LN229 cells after 48 h as observed by nuclear DAPI staining, (A) untreated cells; (B) cells treated with complex **1**; (C) Untreated and complex **1** treated (D) cells from a biological repeat of the same experiment (at 40X magnification),showing nuclear condensation and blebbing indicating apoptotic cells (D). (E) Complex **1** treated cells show an increased caspase 3/7 activity as compared to that of untreated cells using Caspase-Glo® 3/7 assay kit. The graphical data points represent mean ± SD of two independent experiments. Error bars denote ± SD.

Conclusion

We designed two half-sandwich Ru(II)-*p*-cymene complexes with two Schiff base ligands derived from 3-aminoquinoline with 2-hydroxy benzaldehye or 2-hydroxy-1-naphthaldehye. We utilized these complexes to target human glioblastoma LN299 cancer line as possible repurposed chemotherapeutic intervention for GB. The complexes were studied from several spectral and analytical techniques, and the 'piano stool' structure of the complexes was elucidated from X-ray diffraction studies. The complexes undergo solvation in the presence of Tris-buffer and DMF via replacement of labile chloride ligand by the solvent molecules. The complexes were avid binder to CT-DNA, and HSA binding measurement showed preferences for tryptophan-214 (Trp-214) residue. The complexes are photoactive upon illumination of low energy UV-A light (λ_{exc} = 365 nm), which is correlated with photo-induced ligand dissociation. These photoactive complexes may find its application towards photodynamic therapy (PDT) and photoactivated chemotherapy (PACT) considering rich Ru-photochemistry as an alternative modality of GB treatment. The complexes show encouraging inhibition of

glioblastoma (GB) cell lines with moderate selectivity. The higher selectivity for aggressive brain tumor cells may minimize toxic side effects associated with conventional chemoradiotherapy. We observed the desirable outcome of complex **1** displaying significant antiproliferative activity and lowered cellular migratory potential. The mechanistic studies of complex **1** showed the apoptosis of GB cells with nuclear condensation, blebbing and increased caspase 3/7 activity. We are exploring PACT activity and *in vivo* applications for glioblastoma from these compounds.

Experimental Section

Materials and Methods

All chemicals and regents purchased were analytical grade and used directly without any further purifications. Analytical grade solvents were used for spectral studies while a standard method was followed for solvent purification used for synthesis [55]. 2-hydorxy-benzaldehyde and 2-hydorxy-1-naphthaldehyde were received from Merck (Mumbai, India) and Alfa Aesar, respectively. 3-Aminoquinoline purchased from Avra Synthesis Pvt. Ltd., saccharin sodium salt dihydrate from SDFCL (India), $RuCl_3.xH_2O$ from Arora Matthey Pvt. Ltd. (Kolkata, India) and tris-(hydroxymethyl)-aminomethane (Tris) from Merck life science Pvt. Ltd. (Mumbai) India. Tris-HCl-NaCl buffer solution was prepared in Milli-Q water (18.2 MΩ) and stored at 4°C. α-Phellandrene and bioanalytical grade calf thymus (CT) DNA, ethidium bromide (EthB) and human serum albumin (HSA, lyophilized powder, Fatty acid free, Globulin free, ≥99%) were obtained from Sigma Chemicals (U. S. A.). The metal precursor $[(\eta^6\text{–}p\text{-cymene})Ru(\mu\text{-}Cl)Cl]_2$ was prepared from following standard literature procedures from $RuCl_3.xH_2O$ and α-Phellandrene [56]. Elemental analyses were measured from Perkin-Elmer 2400 series-II analyzer. Fourier transform infrared (FTIR) spectral data recorded in KBr pellets from Perkin-Elmer 1320 instrument. Molecular masses were determined from Waters Q-TOF Premier electron spray ionization (ESI-MS) spectrometer. ^1H and ^{13}C NMR recorded in JEOL 400 MHz spectrometer using deuterated solvents as a secondary reference. Absorption spectra and circular dichroism (CD) spectra measured in JASCO V-670 and JASCO J-815 spectrophotometers, respectively. Agilent Cary Eclipse spectrophotometer used for fluorescence measurement.

Synthesis of ligands

The ligands 2-[(*E*)-(3-quinolinylimino)methyl]phenol (L1) and 2-[(*E*)-(3-quinolinylimino)methyl)naphthol were synthesized from modified literature and characterized from reported methods [57, 58]. To the solution of 3-aminoquinline in dry ethanol, 2-hydorxy-benzaldehyde (L1) and 2-hydorxy-1-naphthaldehyde (L2) were added, and the mixture was refluxed for 6 h. The L1 appeared as orange-red and L2 as a yellow color precipitate, which was separated and washed thoroughly with 3 × Et_2O. The single crystal of L2 was obtained from the slow evaporation of a mixture of ethanol and Et_2O at room temperature.

Synthesis of complexes

Complexes [Ru(η^6-*p*-cymene)(L1)Cl] (**1**) and [Ru(η^6-*p*-cymene)(L2)Cl] were synthesized by following a general synthetic procedure. To the [(η^6–*p*-cymene)Ru(μ-Cl)Cl]$_2$ (61.24 mg, 0.10 mM) dissolved in 4 mL $CHCl_3$, the L1 (2 equiv., 49.66 mg, 0.20 mM for complex **1**) or L2 (2 equiv., 59.67 mg, 0.20 mM for complex **2**) ligand dissolved also in $CHCl_3$ was added dropwise and neutralized with single equivalent of methanolic KOH solution. The mixture was warmed at 50 °C for 4 h. The resulting brick red solution was dried in vacuum and washed with 3 × Et_2O. Single-crystals of suitable dimensions of both the complexes were grown in $CHCl_3$, by slow diffusion with n-pentane for complex **1**, while complex **2** crystals obtained with slow evaporation mixed with Et_2O at RT.

[Ru(η^6-*p*-cymene)(L1)Cl] (**1**). Yield: 105 mg (95%). Brick red powder. Anal. Calcd for $C_{26}H_{25}ClN_2ORu$: C, 60.28; H, 4.86; N, 5.41. Found: C, 60.19; H, 4.75; N, 5.34. ESI-MS ($CHCl_3$): *m/z* 483.10 $[M\text{-}Cl^-]^+$ (calc. for $C_{26}H_{25}N_2ORu$: *m/z* 483.10). FT-IR (KBr matrix, ν/cm^{-1}): 3432 (s, br), 3053 (w), 2962 (m), 2925 (w), 2870 (w), 1936 (w), 1606 (vs, sh), 1527 (s, sh), 1492 (m), 1459 (m), 1443 (vs, sh), 1414 (w), 1387 (w), 1360 (m), 1325 (m), 1276 (w), 1262 (w), 1191 (m), 1164 (w), 1147 (s, sh), 1135 (m), 1055 (w), 1028 (m), 989 (w), 930 (w), 898 (m), 863 (w), 801 (w), 785 (m), 752 (vs, sh), 662 (w), 633 (w), 597 (w), 494 (m) [vs, very strong; s, strong; m, medium; w, weak; br, broad; sh; sharp]. ^{1}H NMR (400 MHz, Chloroform-*d*) δ 9.28 (s, 1H, imine-H), 8.43 (d, *J* = 2.1 Hz, 1H, quinolinyl), 8.19 (d, *J* = 8.4 Hz, 1H), 7.92 (d, *J* = 7.9 Hz, 1H), 7.84 (s, 1H), 7.78 (t, *J* = 7.9 Hz, 1H), 7.65 (t, *J* = 7.2 Hz, 1H), 7.31 – 7.22 (m, 1H), 7.05 – 6.97 (m, 2H, phenylenyl), 6.46 (t, *J* = 7.3 Hz, 1H, phenylenyl), 5.38 (d, *J* = 6.1 Hz, 1H, *p*-cym-H), 5.29 (d, *J* = 6.1 Hz, 1H, *p*-cym-H), 5.01 (d, *J* = 5.7 Hz, 1H, *p*-cym-H), 4.24 (d, *J* = 5.7 Hz, 1H, *p*-cym-H), 2.63 (hept, *J* = 6.6, 6.1 Hz, 1H, *i*Pr-CH), 2.14 (s, 3H, *p*-cym-CH_3), 1.17 (d, *J* = 6.9 Hz, 3H, *i*Pr-CH_3), 1.13 (d, *J* = 6.8 Hz, 3H, *i*Pr-CH_3). ^{13}C NMR (100 MHz, Chloroform-*d*) δ 165.80 (imine-H), 165.47 (quinolinyl), 151.41, 147.31, 146.93, 136.33,

135.65, 129.89, 129.61, 128.75, 128.20, 128.03, 127.49, 123.10, 118.30 (phenylenyl), 114.76 (phenylenyl), 101.93 (*p*-cym-C-CH_3), 98.56 (*p*-cym-C-*i*Pr), 86.85 (*p*-cym-CH), 83.52 (*p*-cym-CH), 82.95 (*p*-cym-CH), 80.29 (*p*-cym-CH), 30.63 (*i*Pr-CH), 22.89 (*i*Pr-CH_3), 21.80 (*i*Pr-CH_3), 18.71 (*p*-cym-CH_3). UV- visible in DMF [λ_{max}, nm (ε, $M^{-1}cm^{-1}$)]: 274 (16300), 325 (7800), 447 (2780).

[Ru(η^6-*p*-cymene)(L2)Cl] (2). Yield: 112 mg (93%). Brick red powder. Anal. Calcd for $C_{30}H_{27}ClN_2ORu$: C, 63.43; H, 4.79; N, 4.93. Found: C, 63.36; H, 4.73; N, 4.85. ESI-MS ($CHCl_3$): *m/z* 533.12 $[M\text{-}Cl^-]^+$ (calc. for $C_{30}H_{27}N_2ORu$: *m/z* 533.12). FT-IR (KBr matrix, ν/cm^{-1}): 3430 (vs, br), 2960 (m), 2926 (m), 1935 (w), 1616 (vs, sh), 1603 (vs), 1581 (s), 1535 (s, sh), 1501 (w), 1453 (m), 1429 (s), 1399 (s), 1369 (s), 1188 (m), 1160 (m), 1136 (m), 1031 (w), 999 (w), 970 (w), 859 (w), 827 (m), 784 (w), 750 (s), 645 (w), 618 (m), 480 (w). ^{1}H NMR (400 MHz, Chloroform-*d*) δ 9.33 (s, 1H, imine-H), 8.65 (s, 1H, quinolinyl), 8.43 (s, 1H), 8.22 (d, *J* = 8.3 Hz, 1H), 7.94 (d, *J* = 8.1 Hz, 1H), 7.79 (t, *J* = 7.5 Hz, 1H), 7.71– 7.63 (m, 3H), 7.57 (d, *J* = 7.8 Hz, 1H), 7.33 (t, *J* = 7.6 Hz, 1H, naphthalenyl), 7.17 (dd, *J* = 14.7, 8.2 Hz, 2H, naphthalenyl), 5.43 (d, *J* = 6.0 Hz, 1H, *p*-cym-H), 5.34 (d, *J* = 6.1 Hz, 1H, *p*-cym-H), 5.01 (d, *J* = 5.5 Hz, 1H, *p*-cym-H), 4.28 (d, *J* = 5.5 Hz, 1H, *p*-cym-H), 2.64 (hept, *J* = 6.9, 6.4 Hz, 1H, *i*Pr-CH), 2.17 (s, 3H, *p*-cym-CH_3), 1.18 (d, *J* = 6.9 Hz, 3H, *i*Pr-CH_3), 1.12 (d, *J* = 6.9 Hz, 3H, *i*Pr-CH_3). ^{13}C NMR (100 MHz, Chloroform-*d*) δ 166.95 (imine-H), 158.82 (quinolinyl), 152.47, 148.11, 146.79, 136.75, 134.82, 129.75, 129.61, 129.11, 128.93, 128.19, 127.98, 127.75, 127.63, 126.84, 125.51, 122.42, 118.66 (naphthalenyl), 108.74 (naphthalenyl), 101.84 (*p*-cym-C-CH_3), 98.58 (*p*-cym-C-*i*Pr), 86.88 (*p*-cym-CH), 84.32 (*p*-cym-CH), 83.03 (*p*-cym-CH), 80.54 (*p*-cym-CH), 30.69 (*i*Pr-CH), 22.89 (*i*Pr-CH_3), 21.78 (*i*Pr-CH_3), 18.77 (*p*-cym-CH_3). UV- visible in DMF [λ_{max}, nm (ε, M^{-1} cm^{-1})]: 275 (23730), 323 (11220), 461 (3810).

Solubility and Stability

The complexes were stable in solid-state for several months and non-hygroscopic in nature. The complexes found soluble in MeOH, CH_3CN, DCM, $CHCl_3$, DMF and DMSO and were insoluble in water and aliphatic hydrocarbons (n-pentane and n-hexane). The solution-state stability of the complexes was determined from time-dependent absorption spectral measurement of DMF solution of the complexes; time-dependent ^{1}H NMR scans of DMSO-d_6 solution and ESI-MS spectra in $CHCl_3$ solution. All these time-dependent analyses confirmed the structural integrity of the complexes in the solution.

Single crystal X-ray structure

View Article Online
DOI: 10.1039/D0DT02167A

Red colour and block-shaped crystal of both the complexes were obtained with suitable dimensions at ambient conditions. Data collection was performed on Bruker SMART II diffractometer instrument. The X-ray radiation source used was Mo Kα and data integration was processed from SAINT program [59]. The structure solution was achieved from the direct method using SHELXS program [60, 61], and absorption correction was made from SADABS program [62]. Full matrix least-squares refinement methods were performed combinedly from both the SHELX-2017 [61] and the Olex2 software [63]. The non-hydrogen atoms refinement processed anisotropically for full convergence and hydrogen atoms refinement performed from riding model added for geometry requirement. An ORTEP view of the structures was shown in Fig. 4, the detailed crystallographic parameters given in supporting information. The CCDC deposition identity number for the structures are 2006007 (**1**) and 2006008 (**2**), respectively.

Hydrolysis experiments

The room temperature absorption spectra of the complexes were recorded in Tris-HCl/NaCl buffer (pH = 7.2) for 5 h. The time-dependent absorbance (at 395 nm for **1**, at 379 nm for **2**) was plotted versus time and fitted from origin 8.5 to give monoexponential fit and first-order rate constant k and half-life $t_{1/2}$ from equation (1).

$$A = C_0 + C_1 e^{-kt} \quad \text{.....(1)}$$

where, the absorbance at time t is A and C_0 and C_1 are constant generated from computer fit [64].

Photo-irradiation experiments

The effect of light irradiation (6 W) on solution-state of the complexes was measured from the UV-vis measurement in DMF solution at 298 K. A continuous measurement of absorbance with stipulated experimental time resulted in significant alteration of the electronic spectrum of the samples with the formation of multiple isosbestic point formation. The kinetics of the photochemical changes absorbance at 348 nm (**1**) and 365 nm (**2**) with a function of time. The samples were kept in the dark to avoid any unwanted photochemical reactions.

DNA binding measurements

The binding studies of complexes with CT-DNA were studied from both the absorption and emission techniques. The concentration of DNA was determined from its known molar extinction coefficient (ε = 6600 $M^{-1}cm^{-1}$) [65] and the purity from RNA and protein was

confirmed from the absorbance ratio at 260 nm and 280 nm ~ 1.9 [66]. To the 5mM Tris-HCl/NaCl buffer (pH = 7.2), the solution of the complex (39 μM) in DMF was added to the sample cuvette, and the same volume of DMF to the reference cuvette and absorbance was recorded. The CT-DNA (0–25 μM for (**1**) and 0–15 μM for (**2**)) solution was added to the reference and sample cuvette to eliminate the absorption of DNA itself. The absorption spectra recorded after each addition of DNA and absorbance at 275 nm (**1**) and 273 nm (**2**) used for calculation of binding constant from the following

$$[DNA]/(\varepsilon_a-\varepsilon_f) = [DNA]/(\varepsilon_b-\varepsilon_f) + 1/K_b(\varepsilon_b-\varepsilon_f) \quad \text{..... (2)}$$

where, [DNA] is the concentration of CT-DNA, ε_a and ε_b are molar extinction coefficient for the apparent and fully bound species while ε_f, represents molar extinction coefficient in absence DNA [67]. The ratio of the slope to intercept of linear fitted $[DNA]/(\varepsilon_a - \varepsilon_f)$ vs. [DNA] plots gives the intrinsic equilibrium binding constant (K_b).

The ethidium bromide displacement assay and circular dichroism DNA binding studies were performed by following our recent publication [18].

Protein binding experiments

The binding of the complexes with human serum albumin (HSA) was determined from the fluorescence quenching experiments of tryptophan of the protein and synchronous fluorescence measurements in 0.8% DMF-5mM Tris-HCl/NaCl buffer (pH 7.2) mixture. To the HSA (2.4 μM), the addition of complexes **1** and **2** (0–4 μM) lead to quenching of emission intensity at 346 nm. The Stern-Volmer quenching constant (K_{HSA}) was calculated from the equation (3) by slope of linear fit between I_0/I and [Q] [68]

$$I_0/I = 1 + K_{HSA}[Q] \text{..... (3)}$$

$$I_0/I = 1 + K_q \tau_0 [Q] \text{..... (4)}$$

Where, the quencher (complex) concentration [Q] lead to intensity change from I_0 of HSA to I. The symbols, K_q and τ_0 represents the quenching rate constant and average life time of the HSA (~ 10^{-8} s) in the absence of quencher. Further, the number of binding sites (n) and the binding constant (K) of the complexes **1** and **2** with HSA were measured from the linear fit of the modified Stern-Volmer equation (5) [69].

$$\log(I_0-I)/I = \log K + n\log[Q] \text{.....(5)}$$

The synchronous fluorescence measurement was also recorded after each addition of the complexes to HSA with parameters $\Delta\lambda$ = 15 nm and $\Delta\lambda$ = 60 nm.

Cell culture

View Article Online
DOI: 10.1039/D0DT02167A

The mouse fibroblast cell line (L929) was procured from the cell repository of the National Center for Cell Sciences (NCCS, Pune), India. The human glioblastoma (GB) cell line (LN229) was a kind gift from Dr. Kunzang Chosdol (AIIMS, New Delhi, India). Both the cell lines were maintained in DMEM (GIBCO) media, supplemented with 10% fetal bovine serum (FBS), along with 100U/ml penicillin, and 100 mg/ml streptomycin. The cells were cultured at 37ºC and 5% CO_2 in a humidified atmosphere in an incubator.

Determination of IC_{50} value and antiproliferative activity

The *in-vitro* cytotoxicity of the ruthenium-based compounds and cisplatin was determined by the MTT cell viability assay. The ruthenium-based drugs were dissolved in DMSO, while cisplatin was dissolved in an aqueous solution of 0.9% NaCl due to controversial reports of its chemical structure alteration in DMSO (Hall *et al.,* 2014). Briefly, about 1×10^5 cells of the GB cell line (LN229) or the normal fibroblast cells (L929) were seeded in each well of a 96 well plate, 24 hours prior to treatment. Cells were then treated with various concentrations of drugs and incubated for 24 hours (maximum final concentration of DMSO [70] used was 0.6%) at 37 ºC and 5% CO_2 in an incubator. The following day, media was removed and 100 µl fresh media containing 3-(4,5-dimethylthiazole-2-yl)-2,5-diphenyl tetrazolium bromide) MTT reagent (0.5 mg/ml) was introduced in each well, and the plate was incubated for an additional two hours at 37 ºC in the dark. Tetrazolium crystals formed were dissolved by adding 100 µl of DMSO per well. Absorbance at 595 nm was measured using a microplate reader. The 50% inhibitory concentration (IC_{50}) was determined by plotting the % cell viability against the drug concentration. Data points were collected in triplicate, and each experiment was repeated three times. The % cell viability was calculated using the following formulae:

$$\%\ Cell\ viability = \frac{Absorbance\ (treated) - Absorbance\ (blank)}{Absorbance\ (untreated) - Absorbance\ (blank)} \quad \ldots\ldots\ldots\ (6)$$

Selectivity index (S.I.) of the drug was calculated as follows:

$$S.I. = \frac{IC_{50}\text{ value for normal cell line (L929)}}{IC_{50}\text{ value for GB cell line (LN229)}} \quad \ldots\ldots\ldots\ldots(7)$$

A drug displaying S.I. ≥ 3 is considered to be highly selective towards cancer [71].

To measure the effect of the drug on cellular proliferation, briefly, about 5×10^3 LN229 cells were seeded in each well of a 96 well plate and drug treatment was given at the determined IC_{50} value. The treated and untreated cells were scored at various time points using the above-

mentioned method. Relative proliferation was plotted by comparing the fold change in absorbance values of both the groups as compared to day 0.

Colony formation assay

About 1000 LN229 cells were seeded in each well of a 6-well plate in the presence or absence of the drug and allowed to grow up to two weeks until they form colonies. The colonies were then fixed with 3.7% formaldehyde and stained with crystal violet. The experiment was performed in triplicate and repeated three times. Images of the microscopic colonies, as well as the plate, were captured for comparison purposes.

Wound healing assay

LN229 Cells were seeded in a 12 well plate such that they become nearly 90-100% confluent after 24 hours. The monolayer of cells was scraped with a sterile 200µl pipette tip followed by removal of debris by washing with PBS. Serum-free media was introduced with or without drug and the wound closure process was monitored over a period of 24 hours by capturing image at various time points. The migration was quantified by using an arbitrary unit scale. The experiment was performed three times in triplicate.

Apoptosis assessment by DAPI staining

LN229 cells were seeded in 24-well plates at a seeding density of 1×10^5 cells/well and allowed to grow overnight. The cells were then treated with 22.8 μM of the drug and incubated for 48 hours. After the treatment period, the cells were washed with PBS, and fixed with 3.7% formaldehyde, followed by PBS wash. Next, the cells were permeabilized with 0.2% Triton X-100 and washed with PBS. Finally, the cells were incubated in DAPI labeling solution for 5 minutes at room temperature and imaged under a fluorescent microscope (λ_{ex} ~359 nm, λ_{em} ~ 461 nm). The experiment was repeated three times.

Apoptosis analysis by Caspase 3/7 Glo assay

LN229 cells were subjected to 22.8 μM complex **1** treatment for 48 hours. After drug treatment, 5×10^3 cells from both treated and untreated control group of cells were treated with caspase 3/7 Glo reagent according to manufacturer's instructions (Promega, USA). After an incubation of 1.5 hours at room temperature, luminescence (caspase activity), was recorded using a luminometer (Berthold, Germany). The experiment was repeated twice.

View Article Online
DOI: 10.1039/D0DT02167A

Notes

The authors declare no competing financial interest.

Acknowledgments

The Science and Engineering Research Board (Project number: EMR/2016/000521) is greatly acknowledged for the financial support of this work. P. K. was supported by University Grant Commission (U. G. C.) fellowship. R. K. was supported by internal grant from IIT Delhi for this study. I. M. is thankful to the Ministry of Human Resource and Development (MHRD), Govt. of India for senior research fellowship.

Electronic Supplementary Information (ESI) available:

Characterization data, crystallographic details, additional spectral results for kinetics, DNA/HSA binding. See DOI: xx.xxx/xxxxxxx.

References

1. Bai, R.-Y.; Staedtke, V.; Riggins, G. J. Molecular targeting of glioblastoma:Drug discovery and therapies. *Trends. Mol. Med.* **2011**, *17*, 301−312.
2. (a) Chen, J.; McKay, R. M.; Parada, L. F.; Malignant glioma: lessons from genomics, mouse models, and stem cells. *Cell*. **2012,** *149*, 36−47. (b) Li, S. C.; Vu, L. T.; Ho, H. W.; Yin, H. Z.; Keschrumrus, V.; Lu, Q.; Wang, J.; Zhang, H.; Ma, Z.; Stover, A.; Weiss, J. H.; Schwartz, P. H. Loudon, W. G. Cancer stem cells from a rare form of glioblastoma multiforme involving the neurogenic ventricular wall. *Cancer Cell Int.* **2012**, 12:41
3. Crowley, R.W.; Pouratian, N.; Sheehan, J. P.; Gamma knife surgery for glioblastoma multiforme. *Neurosurgical focus* **2006**, 20(4):E17.
4. Polivka Jr., J.; Polivka, J.; Holubec, L.; Kubikova, T.; Priban, V.; Hes, O.; Pivovarcikova, K.; Treskova, I. Advances in experimental targeted therapy and immunotherapy for patients with glioblastoma multiforme. *Anticancer Res.* **2017**, *37*, 21−34.
5. Wang, M.; Jiang, X.; Wu, F.; Xu, H.; Lin, Z.; Qi, B.; Xia, H. The advances in targeted therapy and immunotherapy for glioblastoma: Basic research and clinical trials. *Glioma* **2018**, *1*, 79−88.
6. Kelland, L. The resurgence of platinum-based cancer chemotherapy, *Nat. Rev.* **2007**, *7* 573−584.

7. McWhinney, S. R.; Goldberg, R. M.; Mc Leod, H. L. Platinum neurotoxicity pharmacogenetics, *Mol. Cancer Ther.* **2009**, *8*, 10−16.
8. Guo, Z.; Sadler, P. J. Metals in medicine. *Angew. Chem. Int. Ed.* **1999**, *11*, 1512−1531.
9. Mjos, K. D.; Orvig, C. Metallodrugs in medicinal inorganic chemistry. *Chem*. *Rev*. **2014**, *114*, 4540−4563.
10. Bergamo, A.; Giaddon, C.; Schellens, J. H. M.; Beijnen, J. H.; Sava, G. Approaching tumour therapy beyond platinum drugs Status of the art and perspectives of ruthenium drug candidates. *J. Inorg. Biochem.* **2012**, *106*, 90−99.
11. (a) Mari, C.; Pierroz, V.; Ferrarib, S.; Gasser, G. Combination of Ru(II) complexes and light: new frontiers in cancer therapy. *Chem. Sci.* **2015**, *6*, 2660−2686. (b) Monro, S.; Colon, K. L.; Yin, H.; Roque, J.; Konda, P.; Gujar, S.; Thummel, R. P.; Lilge, L.; Cameron, C. G.; McFarland, S. A. Transition Metal Complexes and Photodynamic Therapy from a Tumor-Centered Approach: Challenges, Opportunities, and Highlights from the Development of TLD1433. *Chem. Rev.* **2019**, *119*, 797-828.
12. HC Askes, S.; Bahreman, A.; Bonnet, S.; Activation of a photodissociative ruthenium complex by triplet-triplet annihilation upconversion in liposomes. *Angew. Chem. Int. Ed.* **2014**, *53*, 1029−1033.
13. Chen, H.; Parkinson, J. A.; Parsons, S.; Coxall, R. A.; Gould, R. O.; Sadler, P. J. Organometallic ruthenium(II) diamine anticancer complexes: Arene nucleobase stacking and stereospecific hydrogen-bonding in guanine adducts. *J. Am. Chem. Soc.* **2002**, *124*, 3064–3082.
14. Scolaro, C.; Bergamo, A.; Brescacin, L.; Delfino, R.; Cocchietto, M.; Laurenczy, G.; Geldbach, T. J.; Sava, G.; Dyson P. J. In vitro and In Vivo evaluation of ruthenium(II)-arene PTA complexes. *J. Med. Chem.* **2005**, *48*, 4161–4171.
15. Liu, H. -K.; Berners-Price, S. J.; Wang, F.; Parkinson, J. A.; Xu, J.; Bella, J.; Sadler, P. J. Diversity in guanine selective DNA binding modes for an organometallic ruthenium arene complex. *Angew. Chem. Int. Ed.* **2006**, *45*, 8153–8156.
16. Chow, M. J.; Licona, C.; Pastorin, G.; Mellitzer,G.; Ang, W. H.; Gaiddon C. Structural tuning of organoruthenium compounds allows oxidative switch to control ER stress pathways and bypass multidrug resistance. *Chem. Sci*. **2016**, *7*, 4117−4124.
17. Chow, M. J.; Alfiean, M.; Pastorin, G.; Gaiddon, C. Ang, W. H. Apoptosis-independent organoruthenium anticancer complexes that overcome multidrug resistance: self-assembly and phenotypic screening strategies. *Chem. Sci*. **2017**, *8*, 3641−3649.

18. Kumar, P.; Butcher, R.; Patra, A. K. Ternary Co(II), Ni(II) and Cu(II) complexes containing dipyridophenazine and saccharin: Structures, reactivity, binding interactions with biomolecules and DNA damage activity. *Inorg. Chim. Acta* **2020**, *506*, 119532.
19. El-Sonbati, A. Z.; El-Bindary, A. A.; Shoair, A. F. Stereochemistry of new nitrogen containing heterocyclic aldehyde. VIII. Spectral and coordination modes of mixed ligand of novel ruthenium(III) complexes. *Spectrochim. Acta A* 2**002**, *58*, 3003−3009.
20. Bhowon, M. G.; Wah, H. L. K.; Narain, R. Schiff base complexes of ruthenium(II) and their use as catalytic oxidants. *Polyhedron* **1998**, *18*, 341−345.
21. Nazarov, A. A.; Hartinger, C. G.; Dyson, P. J. Opening the lid on piano-stool complexes: An account of ruthenium(II)–arene complexes with medicinal applications. *J. Organomet. Chem.* **2014,** *751*, 251−260.
22. Singh, A. K.; Pandey, D. S.; Xu, Q.; Braunstein, P. Recent advances in supramolecular and biological aspects of ruthenium(II) complexes. *Coord. Chem. Rev*. **2012,** *270-271*, 31−56.
23. Habtemariam, A.; Melchart, M.; Fernández, R.; Parsons, S.; Oswald, I. D. H.; Parkin, A.; Fabbiani, F. P. A.; Davidson, J. E.; Dawson, A.; Aird, R. E.; Jodrell, D. I.; Sadler, P. J. Structure−Activity Relationships for Cytotoxic Ruthenium(II) Arene Complexes Containing N,N-, N,O-, and O,O-Chelating Ligands. *J. Med. Chem.* **2006,** *49*, 6858−6868.
24. Chen, F.; Romero-Canelon, I.; Soldevila-Barreda, J. J.; Song, J. I.; Coverdale, J. P. C.; Clarkson, G. J.; Kasparkova, J.; Habtemariam, A.; Wills, M.; Brabec, V.; Sadler, P. J. Transfer Hydrogenation and Antiproliferative Activity of Tethered Half-Sandwich Organoruthenium Catalysts. *Organometallics* **2018,** *37*, 1555−1566.
25. Acharya, S.; Maji, M.; Ruturaj; Purkait, K.; Gupta, A.; Mukherjee, A. Synthesis, Structure, Stability, and Inhibition of Tubulin Polymerization by Ru^{II}–*p*-Cymene Complexes of Trimethoxyaniline-Based Schiff Bases. *Inorg. Chem.* **2019**, *58*, 9213−9224
26. Howe-Grant, M. E.; Lippard, S. J. *Metal Ions in Biological Systems*. Sigel, H., Ed.; Marcel Dekker: New York,: **1980**; Vol.11, 63−125.
27. Frey, U.; Ranford, J. D.; Sadler, P. J. Ring-opening reactions of the anticancer drug carboplatin: NMR characterization of cis-[$Pt(NH_3)_2$(CBDCA-O)(5'-GMP-N7)] in solution. *Inorg. Chem.* **1993,** *32*, 1333−1340.

28. Zhao, J.; Li, W.; Gou, S.; Li, S.; Lin, S.; Wei, Q.; Xu, G. Hypoxia-Targeting Organometallic Ru(II)–Arene Complexes with Enhanced Anticancer Activity in Hypoxic Cancer Cells. *Inorg. Chem.* **2018,** *57*, 8396−8403.
29. Wang, F.; Habtemariam, A.; van der Geer, E. P. L.; Fernández, R.; Melchart, M.; Deeth, R. J.; Aird, R.; Guichard, S.; Fabbiani, F. P. A.; Lozano-Casal, P.; Oswald, I. D. H.; Jodrell, D. I.; Parsons, S.; Sadler, P. J. Controlling ligand substitution reactions of organometallic complexes: Tuning cancer cell cytotoxicity. *P. Natl. Acad. Sci. U. S. A.* **2005,** *102*, 18269−18274.
30. Mukherjee, A.; Acharya, S.; Purkait, K.; Chakraborty, K.; Bhattacharjee, A.; Mukherjee, A. Effect of *N*,*N* Coordination and Ru^{II} Halide Bond in Enhancing Selective Toxicity of a Tyramine-Based Ru^{II} (*p*-Cymene) Complex. *Inorg. Chem.* **2020**, *59*, 6581−6594.
31. Dadci, L.; Elias, H.; Frey, U.; Hoernig, A.; Koelle, U.; Merbach, A. E.; Paulus, H.; Schneider, J. S. .pi.-Arene Aqua Complexes of Cobalt, Rhodium, Iridium, and Ruthenium: Preparation, Structure, and Kinetics of Water Exchange and Water Substitution. *Inorg. Chem.* **1995,** *34*, 306−315.
32. Miller, S. E.; House, D. A. The hydrolysis products of cis diamminedichloroplatinum(II) 5. The anation kinetics of cis-$Pt(X)(NH_3)_2(OH_2)$+ (X=Cl, OH) with glycine, monohydrogen malonate and chloride. *Inorg. Chim. Acta* **1991,** *187*, 125−132.
33. Koziar, J. C.; Cowan, D. O. Photochemical heavy-atom effects. *Acc. Chem. Res.* **1978,** *11*, 334−341.
34. Knoll, J. D.; Turro, C. Control and utilization of ruthenium and rhodium metal complex excited states for photoactivated cancer therapy. *Coord. Chem. Rev.* **2015,** *282−283*, 110−126.
35. Betanzos-Lara, S.; Salassa, L.; Habtemariam, A.; Novakova, O.; Pizarro, A. M.; Clarkson, G. J.; Liskova, B.; Brabec, V.; Sadler, P. J. Photoactivatable Organometallic Pyridyl Ruthenium(II) Arene Complexes. *Organmetallic*, **2012**, *31*, 3466−3479.
36. Pal, M.; Nandi, U.; Mukherjee, D. Detailed account on activation mechanisms of ruthenium coordination complexes and their role as antineoplastic agents. *Eur J. Med. Chem.* **2018**, *150*, 419−445.
37. Howerton, B.S.; Heidary, D. K.; Glazer, E.C. Strained ruthenium complexes are potent light-activated anticancer agents, *J. Am. Chem. Soc.* **2012,** *134*, 8324−8327.
38. Goldbach, R. E.; Rodriguez-Garcia, I.; van Lenthe, J. H.; Siegler, M. A.; Bonnet, S. N-Acetylmethionine and Biotin as Photocleavable Protective Groups for Ruthenium Polypyridyl Complexes. *Chem. -Eur. J.* **2011**, *17*, 9924−9929.

39. Barragán, F.; López-Senín, P.; Salassa, L.; Betanzos-Lara, S.; Habtemariam, A.; Moreno, V.; Sadler, P. J.; Marchán V. Photocontrolled DNA Binding of a Receptor-Targeted Organometallic Ruthenium(II) Complex. *J. Am. Chem. Soc.* **2011**, *133*, 14098–14108.

40. (a) Johnstone, T. C.; Suntharalingam, K.; Lippard, S. J. The Next Generation of Platinum Drugs: Targeted Pt(II) Agents, Nanoparticle Delivery, and Pt(IV) Prodrugs. *Chem. Rev.* **2016,** *116*, 3436−3486. (b) Bergamo, A.; Dyson, P. J.; Sava, G. The mechanism of tumour cell death by metal-based anticancer drugs is not only a matter of DNA interactions. *Coord. Chem. Rev.* **2018**, *360*, 17−33.

41. Novakova, O.; Chen, H.; Vrana, O.; Rodger, A.; Sadler, P. J.; Brabec, V. DNA Interactions of Monofunctional Organometallic Ruthenium(II) Antitumor Complexes in Cell-free Media. *Biochemistry* **2003,** *42*, 11544−11554.

42. Kelly, J. M.; Tossi, A. B.; McConnell, D. J.; OhUigin, C. A study of the interactions of some polypyridylruthenium(II) complexes with DNA using fluorescence spectroscopy, topoisomerisation and thermal denaturation. *Nucleic Acids Res.* **1985,** *13*, 6017−6034.

43. (a) Waring, M. J. Complex formation between ethidium bromide and nucleic acids. *J. Mol. Biol.* **1965,** *13*, 269−282. (b) Kumar, P.; Dasari, S.; Patra, A. K. Ruthenium(II) complexes of saccharin with dipyridoquinoxaline and dipyridophenazine: Structures, biological interactions and photoinduced DNA damage activity. *Eur. J. Med. Chem.* **2017**, *136*, 52−62.

44. (a) Ghuman, J.; Zunszain, P. A.; Petitpas, I.; Bhattacharya, A. A.; Otagiri, M.; Curry, S. Structural Basis of the Drug-binding Specificity of Human Serum Albumin. *J. Mol. Biol.* **2005,** *353*, 38−52. (b) Kumar, P.; Swagatika, S.; Dasari, S.; Tomar, R. S.; Patra, A. K. Modulation of Ruthenium Anticancer Drugs Analogs with Tolfenamic Acid: Reactivity, Biological Interactions and Growth Inhibition of Yeast Cell. *J. Inrog. Biochem.* **2019**, *199*, 110769.

45. Bickel, U.; Yoshikawa, T.; Pardridge, W. M. Delivery of peptides and proteins through the blood–brain barrier. *Adv. Drug Deliv. Rev.* **2001,** *46*, 247−279.

46. He, X. M.; Carter, D. C. Atomic structure and chemistry of human serum albumin. *Nature* **1992,** *358*, 209−215.

47. Webb, M. I.; Walsby, C. J. Control of ligand-exchange processes and the oxidation state of the antimetastatic Ru(III) complex NAMI-A by interactions with human serum albumin. *Dalton Trans.* **2011,** *40*, 1322−1331.

48. Liu, M.; Lim, Z. J.; Gwee, Y. Y.; Levina, A.; Lay, P. A. Characterization of a Ruthenium(III)/NAMI-A Adduct with Bovine Serum Albumin that Exhibits a High Anti-Metastatic Activity. *Angew. Chem. Int. Ed.* **2010,** *49*, 1661−1664.
49. Bijelic, A.; Theiner, S.; Keppler, B. K.; Rompel, A. X-ray Structure Analysis of Indazolium trans-[Tetrachlorobis(1H-indazole)ruthenate(III)] (KP1019) Bound to Human Serum Albumin Reveals Two Ruthenium Binding Sites and Provides Insights into the Drug Binding Mechanism. *J. Med. Chem.* **2016,** *59*, 5894−5903.
50. Hu, W.; Luo, Q.; Ma, X.; Wu, K.; Liu, J.; Chen, Y.; Xiong, S.; Wang, J.; Sadler, P. J.; Wang, F. Arene Control over Thiolate to Sulfinate Oxidation in Albumin by Organometallic Ruthenium Anticancer Complexes. *Chem. Eur. J.* **2009,** *15*, 6586−6594.
51. Rabbani, G.; Lee, E. J.; Ahmad, K.; Baig, M. H.; Choi, I. Binding of Tolperisone Hydrochloride with Human Serum Albumin: Effects on the Conformation, Thermodynamics, and Activity of HSA. *Mol. Pharmaceut.* **2018,** *15*, 1445−1456.
52. Zhang, G.; Que, Q.; Pan, J.; Guo, J. Study of the interaction between icariin and human serum albumin by fluorescence spectroscopy. *J. Mol. Struct*. **2008**, *881*, 132−138.
53. Bergamo, A.; Sava, G. Linking the future of anticancer metal-complexes to the therapy of tumour metastases. *Chem. Soc. Rev.* **2015**, *44*, 8818−8835.
54. Suzuki, Y.; Nakabayashi, Y.; Takahashi, R. Ubiquitin-protein ligase activity of X-linked inhibitor of apoptosis protein promotes proteasomal degradation of caspase-3 and enhances its anti-apoptotic effect in Fas-induced cell death. *Proc. Natl. Acad. Sci. U.S.A.* **2001***, 98,* 8662−8667.
55. Armarego, W. L. F. *Purification of Laboratory Chemicals, 8th Edition*. Butterworth-Heinemann: 2017; p 1198.
56. Bennett, M. A.; Smith, A. K. Arene ruthenium(II) complexes formed by dehydrogenation of cyclohexadienes with ruthenium(III) trichloride. *J. Chem. Soc., Dalton Trans.* **1974**, 231−241.
57. Al-Allaf, T. A. K.; Sheet, A. Z. M. Platinum group metal Schiff base complexes—I. Platinum complexes. *Polyhedron* **1995,** *14*, 239−248.
58. Roy, A.; Dey, S.; Roy, P. A ratiometric chemosensor for Al^{3+} based on naphthalene-quinoline conjugate with the resultant complex as secondary sensor for F^{-}: Interpretation of molecular logic gates. *Sens. and Actuators B-Chem.* **2016,** *237*, 628-642.
59. *APEX2 V2012.4, Bruker AXS Inc.* Madison: USA, 2012.
60. Sheldrick, G. M. *SHELXL-2014: Program for Crystal Structure Refinement*. University of Göttingen: Göttingen, Germany: 2014.

61. Sheldrick, G. M. Crystal structure refinement with SHELXL. *Acta Cryst. C* **2015**, *71*, 3−8.
62. Sheldrick, G. M. *SADABS, Area Detector Absorption Correction*. University of Göttingen, Göttingen, Germany: 2001.
63. Dolomanov, O. V.; Bourhis, L. J.; Gildea, R. J.; Howard, J. A. K.; Puschmann, H. OLEX2: a complete structure solution, refinement and analysis program. *J. Appl. Crystallogr.* **2009,** *42*, 339−341.
64. Dougan, S. J.; Melchart, M.; Habtemariam, A.; Parsons, S.; Sadler, P. J. Phenylazo-pyridine and phenylazo-pyrazole chlorido ruthenium(II) arene complexes: Arene loss, aquation, and cancer cell cytotoxicity. *Inorg. Chem*. **2006**, *45*, 10882−10894.
65. Reichmann, M. E.; Rice, C. A.; Thomas, C. A.; Doty, P. A further examination of the molecular weight and size of deoxypentose nucleic acid. *J. Am. Chem. Soc.* **1954,** *76*, 3047−3053.
66. Marmur, J. A procedure for the isolation of deoxyribonucleic acid from microörganisms. *J. Mol. Biol.* **1961,** *3*, 208−218.
67. Wolfe, A.; Shimer, G. H., Jr.; Meehan, T. Polycyclic aromatic hydrocarbons physically intercalate into duplex regions of denatured DNA. *Biochemistry* **1987,** *26*, 6392−6396.
68. Lakowicz, J. R. *Principles of Fluorescence Spectroscopy*. 3rd ed.; Springer New York, 2006.
69. Scatchard, G. The attraction of proteins for small molecules and ions. *Ann. N. Y. Acad. Sci.* **1949,** *51*, 660−672.
70. Hall, M. D.; Telma, K. A.; Chang, K. E.; Lee, T. D.; Madigan, J. P.; Lloyd, J. R.; Goldlust, I.S.; Hoeschele, J. D.; Gottesman, M. M.; Say no to DMSO: dimethylsulfoxide inactivates cisplatin, carboplatin, and other platinum complexes. *Cancer res*. **2014**, 74, 3913−3922.
71. Skiera, I.; Antoszczak, M.; Trynda, J.; Wietrzyk, J.; Boratyński, P.; Kacprzak, K.; Huczyński, A. Antiproliferative activity of polyether antibiotic–Cinchona alkaloid conjugates obtained *via* click chemistry. *Chem. Biol. drug Des*. **2015**, *86*, 911−917.

TOC Graphic

View Article Online
DOI: 10.1039/D0DT02167A

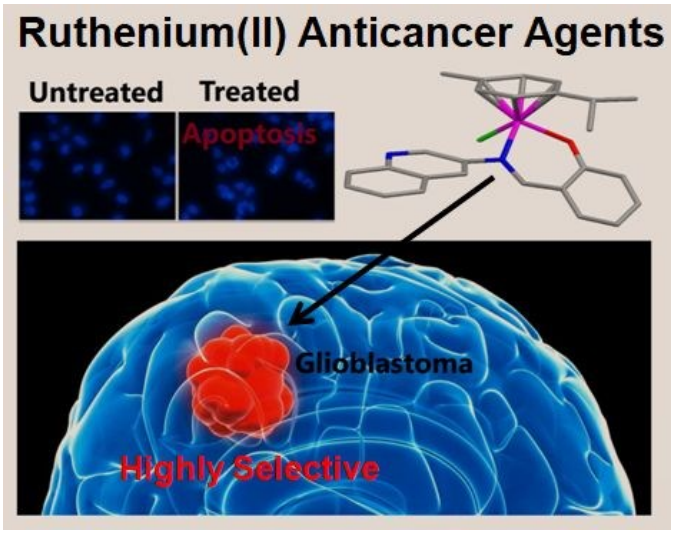

Synopsis: Two bioactive Ru(II)-*p*-cymene complexes were designed, structurally analysed, and investigated its therapeutic potential against *in vitro* human glioblastoma (GB) cells.

TOC Graphic

View Article Online
DOI: 10.1039/D0DT02167A

Synopsis: Two bioactive Ru(II)-*p*-cymene complexes were designed, structurally analysed, and investigated its therapeutic potential against *in vitro* human glioblastoma (GBM) cells.